UNIVERSITY OF CALIFORNIA

Los Angeles

Broadband Enhanced Resonance of

Vanadium Oxide Variable Emissive Multilayer

A thesis submitted in partial satisfaction

of the requirements for the degree Masters of Science

in Material Science and Engineering

by

Samuel Lowell Dunscombe

2023

ABSTRACT OF THE THESIS

Broadband Enhanced Resonance of

Vanadium Oxide Variable Emissive Multilayer

by

Samuel Lowell Dunscombe

Masters of Science in Materials Science and Engineering

University of California, Los Angeles, 2023

Professor Aaswath Raman, Chair

VO_2 is a thermochromic material that has been historically incorporated in variable emissive multilayer (VEM) designs for passive thermal management. However, this remains a relatively nascent research area, and limited efforts have been directed towards optimizing the Fabry-Perot resonance VO_2-based VEM design. This study presents the synthesis and characterization of VO_2 films deposited using magnetron sputtering. The change in emittance ($\Delta\epsilon$) of VEM designs, incorporating silicon or silicon oxide spacer layers on silver reflectors, are documented. The study showcases the optimization of the VEM design, achieving a notable normal $\Delta\epsilon$ of 0.81 with just a single layer of VO_2. Additionally, enhancement layers to the VEM design are explored and experimentally detailed, demonstrating improvements in $\Delta\epsilon$ through broadband enhanced resonance.

The thesis of Samuel Lowell Dunscombe is approved.

Qibing Pei

Jenn-Ming Yang

Aaswath Raman, Committee Chair

University of California, Los Angeles

2023

Table of Contents

List of Figures

List of Tables

Acknowledgements

I would like to acknowledge the support and contribution of several individuals, without whose assistance and mentorship this would not be possible.

At Aerospace Corporation, I would like to thank Dr. Peter Fuqua and Dr. James Barrie for their constant guidance, mentorship, and invaluable expertise. I would like to thank Mr. Paul Adams for his support on XRD characterization and Dr. Hyun Kim for his assistance with XPS analysis. I would like to thank Dr. Chelsea Appleget and Mr. Frank Pan for their advice, help, and much needed encouragement. I would like to thank my managers past and present: Dr. Tim Graves, Dr. Linton Honda, Dr. James Nokes, Dr. Kelsey Folgner and Dr. Shant Kenderian for their support. Finally, I would like to thank everyone at the Thin Films group for making the lab a place we can share research and laughs.

From UCLA, I would like to thank my advisor, Professor Aaswath Raman, for his ingenuity and inspiration. Thank you to Mr. David Abraham for your critical work on the MATLAB optimization. I would also like to thank Professor Qibing Pei and Professor Jenn-Ming Yang for their service on my thesis committee.

This research was funded by The Aerospace Corporation's Independent Research and Development (IRAD) program. A version of this thesis is in preparation for publication.

1. Introduction

Recently there has been a renewed interested in passive radiative cooling coatings for thermal control applications [1, 2]. Passive radiative cooling coatings are materials designed to emit thermal radiation efficiently in the infrared spectrum, allowing objects to cool down by radiating heat into the surrounding space. These coatings typically have specific properties that enhance their ability to radiate heat effectively. They are engineered to have high emissivity in the infrared region, meaning they can emit a large proportion of the thermal radiation they absorb. Additionally, they have low absorptivity in the solar spectrum, which prevents them from absorbing too much sunlight and heating up.

While the properties of these static thermal coatings are sufficient, there is a desire for adaptive radiative coatings which can vary emittance of thermal radiation, and thus vary cooling power, based on the temperature of the coating in a variable environment [3, 4]. An adaptive radiative coating like this could exhibit variable emittance. At lower temperatures, the coating would minimize emittance to restrict thermal emission loss and prevent further temperature decrease. Conversely, at higher temperatures, the coating would enhance emittance, fostering a radiative cooling effect to reduce the overall temperature. This variable thermal emittance characteristic would prove beneficial for various applications, including both spacecraft [5-8] and building thermal management [3, 9, 10].

Coatings can be tailored to achieve static desired radiative properties such as high or low emittance through multilayer design, but switchable radiative properties are harder to achieve. One solution to this problem is the incorporation of a thermochromic material in the coating design such a Vanadium Dioxide.

Vanadium Dioxide, VO_2, can exhibit metal to insulator phase transition (MIT) at 68 °C causing the material's resistivity and optical properties to exhibit a significant change [11]. The dramatic change in the electrical and optical properties of thermochromic VO_2 has been studied for use in a variety of applications including Mott memory [12], field effect transistors [13], electrical oscillators [14], mechanical sensors [15], high speed RF-microwave switches [16], THz devices [17], and optical switches [18]. All utilize the metal to insulator phase transition of the VO_2 material by incorporating it into a device structure.

The transition from a metal to an insulator phase in VO_2 makes it well-suited for adaptive radiative coatings. Experimental findings demonstrate that VO_2 variable emissive multilayer (VEM) coatings can achieve a sevenfold variation in radiative cooling power through the implementation of a Fabry-Perot resonance multilayer design [6]. VO_2 based VEM designs have been reported to experimental achieve emittance changes ($\Delta\epsilon$) up 0.66 while theoretical designs have been proposed that achieve emittance changes of 0.78 [19]. While the theoretical studies indicate significant potential for adaptive radiative cooling using VO_2 thin films, challenges persist in the fabrication and experimental demonstrations of these devices.

This study will cover the fabrication, structural and optical characterization, and experimental demonstration of several VO_2-based multilayer coating designs which demonstrate variable emittance for adaptive radiative cooling. The VEM design will be optimized and a novel enhancement layer to the Fabry-Perot design will be proposed and experimentally demonstrated that increases $\Delta\epsilon$ through broadband enhanced resonance.

2. Background and Theory

2.1 Vanadium Oxide and phases

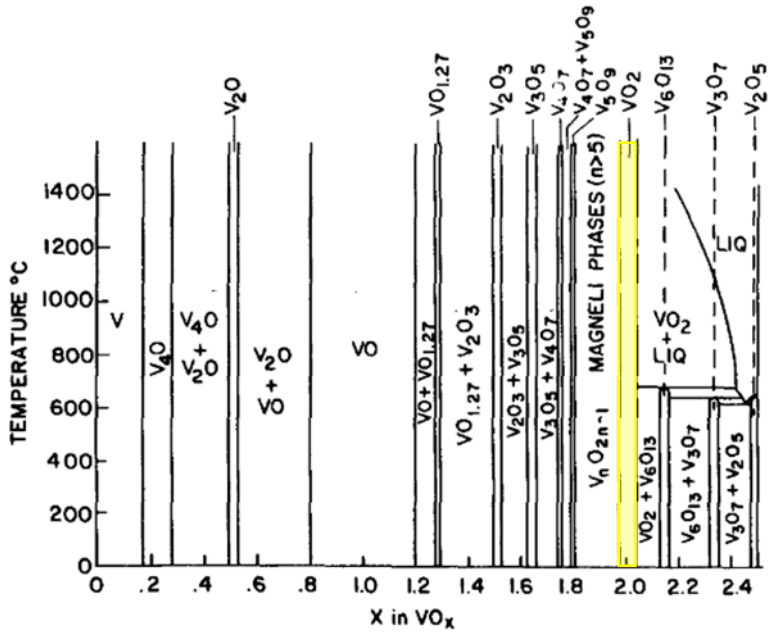

Figure 1: Rough phase diagram of the vanadium oxygen system with VO_2 highlighted [20]. From *Influence of stoichiometry on the metal-semiconductor transition in vanadium dioxide* by C. H. Griffiths et al. J. Appl. Phys. 1974. Copyright 2003 by C. H. Griffiths. Reprinted with permission.

As illustrated in Figure 1, Vanadium oxide exhibits a wide array of stable phases, including V_2O_5, V_2O_3, and V_6O_{13} [20]. This diversity renders it a highly valuable material for numerous industries, but it also poses challenges when attempting to synthesize pure thermochromic VO_2. Throughout the exploration of thermochromic VO_2, VO_2 will frequently be characterized as it being in a high-temperature metallic phase or a low-temperature insulating phase.

As depicted in Figure 2, the high temperature metallic VO_2(R) phase has a tetragonal rutile structure and the low temperature insulating VO_2(M) phase has a monoclinic structure [21,

22]. The high temperature tetragonal rutile phase has V-V pairing separations of 0.287 nm. When it transitions to the low temperature monoclinic phase the pairing is tilted along the c axis causing a doubling in size of the unit cell and alternating V-V separations of 0.285nm and 0.312nm. The d-electrons of each V atom are bound to these V-V bonds. In the high temperature phase the $3d$ electron orbital bands overlap close to the Fermi level causing conduction like a metal. In the low temperature phase the bands split causing a 0.7 eV bandgap as depicted in Figure 3**.** Whether the structural transformation of the V-V dimer triggers the insulating behavior of the VO_2 at low temperature as expected for a Peierls insulator, or the electron correlation effect dominates, as with Mott-Hubbard insulators[23], is still a subject to extensive debate [24-27].

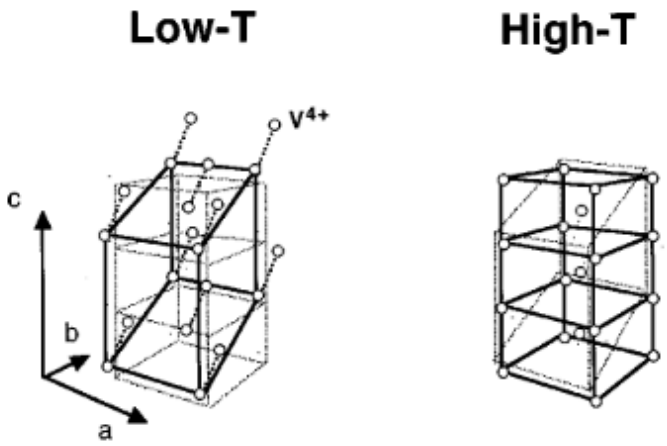

Figure 2: Structural phase VO_2. The Low-T phase is monoclinic. The High-T phase is rutile, tetragonal. The Low T phase is derived after pairing and tilting along the c axis causing its unit cell to be of double the size with distorted oxygen cages [21]. From *Evidence for a structurally-driven insulator-to-metal transition in* VO_2 from A. Cavalleri et al. Phys. Rev. B 2004. Copyright by A. Cavalleri. Reprinted with permission.

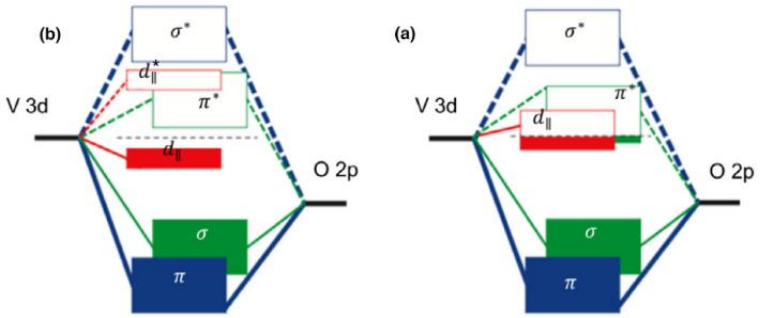

Figure 3: Electronic band structure of a)Monoclinic Insulating and b) Rutile metallic phases of VO_2 [25]. From *Recent progresses on physics and applications of vanadium dioxide* by Kai Liu et al. Materials Today, 2018. Copyright Kai Liu 2018. Reprinted with permission.

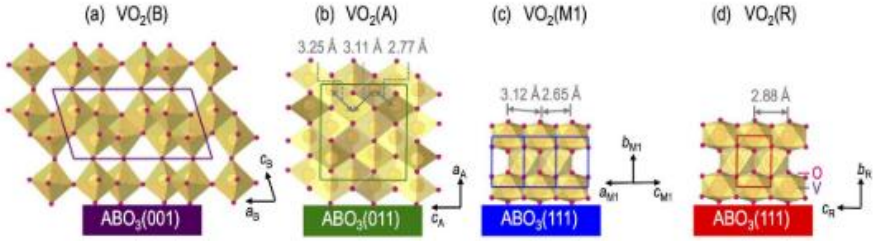

Figure 4: Schematics of (a) VO_2(B), (b) VO_2(A), (c) VO_2(M1) and (d) VO_2(R) phases [28].

Vanadium dioxide, VO_2, has several phases that are not thermochromic as well, such as VO_2(B) and VO_2(A) as illustrated in Figure 4. This becomes important during synthesis when the correct oxygen to vanadium stoichiometry is achieved but the reaction temperature is not enough to produce thermochromic VO_2(M). While Vanadium can be annealed to oxidize or reduce oxygen content or annealed to crystallize to achieve VO_2(M), the aim of this study was to sputter pure VO_2(M) without postprocessing.

2.2 Transition Properties of VO2

The phase change of VO_2 from rutile to monoclinic has electrical [29], thermal [30], and optical [31] changes that are of interest for many applications. This study will center on examining the phase change of VO_2 induced by temperature but it is important to note that a shift in the VO_2 phase can also be initiated by optical [32], mechanical [15] and electrical excitations [33].

It has been observed that during the phase transition from an insulator to a metal, the resistivity of VO_2 could decrease by 4-5 orders of magnitude [11]. Subsequently, it was found that this phase transition is accompanied by a significant transformation in the infrared spectral response. In its insulating phase, VO_2 allows for high infrared transmission, whereas in its metallic phase, it becomes highly absorbing and reflective [31]. This characteristic makes VO_2 particularly appealing for applications related to smart windows [34-37]. These applications require the coating to be transparent to infrared solar wavelengths when it's cold and opaque when it's hot. As will delve into later in this discussion, the infrared transmissive and reflective properties of VO_2 can also be effectively utilized in a multi-layer design for use as a smart radiator with low emissivity at low temperatures and high emissivity at high temperatures.

2.3 Modification of Transition Properties

The control of VO_2's transition properties plays a pivotal role in various applications. When VO_2 undergoes the shift from an insulating to a metallic phase, it creates a difference in optical characteristics known as the transition amplitude. The transition temperature, situated at the midpoint of this amplitude during the heating process, and the variance in transition

temperature between heating and cooling collectively establish a hysteresis curve, all of which are visually represented in Figure 5.

These parameters, namely the transition temperature, amplitude, and hysteresis width, are of paramount importance across a range of applications and necessitate precise management. Fortunately, it is feasible to fine-tune the optical switching amplitude, hysteresis width, and transition temperature of VO_2 using techniques like adjusting film thickness, applying stress, strain, and introducing dopants.

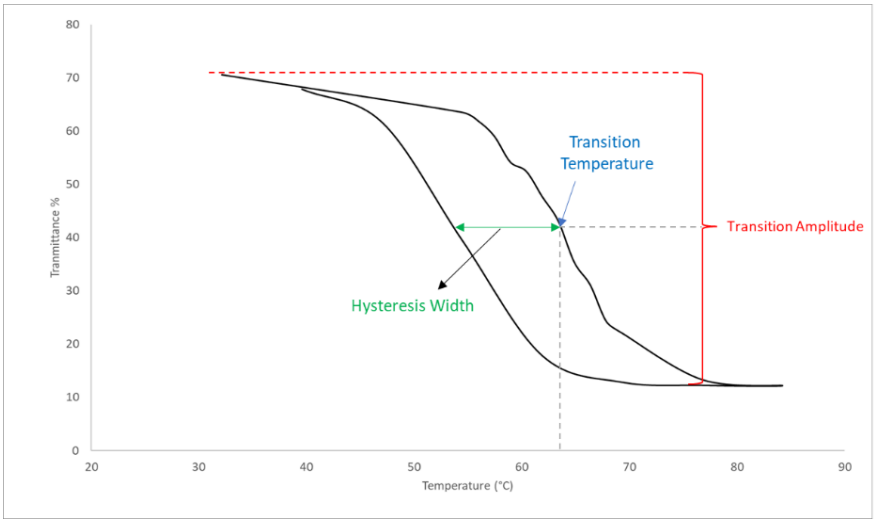

Figure 5: Example transmittance graph labeling Transition Amplitude, Temperature and Hysteresis width of a hysteresis curve.

Thinner VO_2 films (3-25nm) exhibit lower transition temperatures, degraded transition amplitudes, and larger hysteresis widths due to structural defects, film stress and strain between the VO_2 film and the substrate due to thermal expansion coefficient and lattice mismatch respectively [38-42]. As film thickness increases, the strain relaxes and the hysteresis width decreases while transition amplitude increases [38, 43, 44]. This strain effect can be used to tune the transition temperature using buffer layers [41].

VO_2 transition temperature can also be shifted to higher or lower temperatures with introduction of dopants [45]. Ti and Ge are known to the shift VO_2 to a higher temperature, while W, Mo, Nb, Ni, Co and Fe are observed to decrease the transition temperature[45]. This change in transition temperature is due to distortion of the crystal lattice and electron orbitals [27, 45-47]. The exact method by which each dopant affects the transition temperature is still a subject of extensive research and general rules based on donor-like or acceptor-like dopants with large or small ionic radii cannot be uniformly applied to VO_2 thin films [48]. Most radiator applications using VO_2 wish to lower the transition temperature and tungsten is the most effective dopant in reducing transition temperature per atomic basis so it the mostly commonly used [49].

Using the above tools, the transition properties of VO_2 films such as the transition temperature can be honed for specific applications and requirements.

2.4 Synthesis of VO2

Thermochromic VO_2 thin films have been synthesized in a variety of techniques including solution-based depositions such a Sol-gel [26, 50], gas based depositions such a Pulsed Laser Deposition (PLD), Chemical Vapor Deposition (CVD), and the technique that this thesis will employ, sputtering.

The sol-gel method involves metal alkoxides formed into a colloidal solution which is then dipped or spun into a thin film and then dried to remove the liquid phase. As sol-gel does not require large expensive vacuum reactors and manifolds, its wide adoption is mostly due to its low cost. The sol-gel method for depositing VO_2 always requires a thermal annealing step to reach the correct VO_2(M) crystal phase and it also serves to change the porosity of the film

which can be controlled through time and temperature of the anneal [51]. The largest downside of sol-gel is that it is very time-consuming multi-step process.

Chemical vapor deposition (CVD) involves exposing volatile precursors to react and form a film on a substrate while by-products are removed by gas flow. The CVD growth of VO_2 has been exhibited with many different reactants and carrier gases with and without post process annealing at varied pressures from atmospheric to high vacuum [51, 52]. However, CVD does come with certain limitations, including the complexity of ensuring chemical reactions, the use of potentially hazardous precursors, and the formation of heterogeneous and porous films.

Pulsed Laser Deposition (PLD) represents one of the most recent advancements in the fabrication of VO_2 thin films and has proven to be exceptionally well-suited for oxide growth. PLD utilizes a high-powered pulsed laser to vaporize a target material, ensuring stoichiometric deposition onto a substrate. This technique has demonstrated remarkable success in depositing VO_2 films and has even accomplished this without the need for substrate heating or subsequent annealing, a feat that no other gas-based deposition method has achieved [53, 54].

Sputtering of VO_2 is well studied and involves accelerating ions out of a gas plasma discharge to bombard a target material onto a substrate forming a thin film [49, 55]. Sputtering offers a significant advantage in that it enables the deposition of dense, high-quality films at lower temperatures due to the energetic nature of the deposition process. Sputtering parameters such as temperature and oxygen partial pressure effect on the structural, optical, and electrical properties of VO_2 have been studied at length [20, 56, 57]. Optimizing sputtering conditions are an active area of research interest, promising better VO_2 transition properties and lower required substrate temperatures [58].

As previously discussed, there are many stable and metastable phases in the vanadium-oxygen system which makes the role of oxygen partial pressure a key parameter during sputter deposition and critical to achieve thermochromic VO_2(M). Above a critical temperature, small changes in oxygen partial pressure can drastically change the deposited film stoichiometry. When oxygen partial pressure is varied, different mixes of the vanadium oxide phases can be found in the deposited film and the lattice spacing of the VO_2(M) and energy band structure varies due to defects from interstitials and vacancies degrading the switching amplitude [20, 59]. For many vanadium sputtering processes, VO_2 films are obtained in a narrow range of oxygen partial pressure, corresponding to condition where “poisoning” of the cathode (also called a sputtering target) is just starting to occur [60].

The substrate temperature plays a pivotal role in sputtered VO_2 films. In broad terms, research has shown that VO_2 films deposited at temperatures of 350°C, 400°C, and higher tend to exhibit pronounced thermochromism [57, 61], whereas films deposited at 300°C or lower display weak or no thermochromic behavior. However, it's important to note that the specific outcome can vary on a case-by-case basis, influenced by factors such as chamber geometry and sputtering power.

Doping of VO_2 via sputtering can be achieved either by sputtering a single doped vanadium target, or by co-sputtering of two separate targets. Co-sputtering of vanadium and tungsten has resulted in a 23°C decrease in the transition temperature per atomic percent tungsten (23°C/at%) [49]. Molybdenum doping shows a decrease of 12-15°C/at% decrease in transition temperature for doping less than 2 at% [62, 63]

2.5 Characterization of VO2

2.5.1 Structural Characterization

In the study of thermochromic VO_2, structural characterization plays a vital role by enabling the identification of the film's stoichiometry and revealing defects and dopants that have a direct impact on critical thermochromic properties, including switching amplitude, transition temperature, and hysteresis.

X-ray Diffraction (XRD) is a powerful structural characterization technique used to determine the crystallographic structure of materials. It works by measuring the angles and intensities of X-ray beams scattered by a sample, providing information about the arrangement of atoms in a crystalline material, including unit cell parameters, crystal orientation, and phase composition. XRD of crystalline vanadium oxide films determine the stoichiometry of the film by identifying intensity peaks that correspond to unit cell lattice parameters of V_2O_3, VO_2, V_2O_5 and other stable phases [53, 64]. This is also used to determine crystal structure of various polymorph with same stoichiometry such as VO_2(A), VO_2(B) and thermochromic VO_2(M) and VO_2(R).

X-ray Photoelectron Spectroscopy (XPS) is a structural characterization technique that uses X-rays to excite photoelectrons to be ejected from the inner shells of atoms in the material of study. The energy of photoelectrons emitted from the surface of a material is characteristic of the binding energy levels of the electrons in the atoms providing information about the elemental composition, chemical states, and concentrations of elements on the material's surface. XPS is used to determine the stoichiometry of vanadium oxide films by measuring the binding energy of photoelectrons to determine the oxidation state of vanadium atoms from which they were emitted

[64]. This is also used to measure elemental concentrations of dopants in the vanadium oxide films.

Scanning Electron Microscopy (SEM) is another technique for characterizing surface structures. It operates by scanning a focused electron beam across a specimen and detecting the resulting secondary and backscattered electron signals. These signals are harnessed to generate high-resolution images, unveiling details about the sample's surface morphology and composition. SEM images of vanadium oxide films are used to study the surface grain size and thus defect size of the surface grain boundaries [65]. Increasing grain size have been observed to provide higher transition amplitudes and decreased hysteresis width due to decreased grain boundary defects [65-67].

Structural characterization is crucial for optimizing VO_2 synthesis conditions to deposit films with precise stoichiometry, crystal structure and defects size.

2.5.2 Optical Characterization

Comprehensive optical characterization is essential for quantifying the optical transition amplitude, transition temperature, and hysteresis width of VO_2 films. It is paramount for predicting and understanding the behavior of VO_2 films within intricate multilayer structures, making a deep dive into the intricacies of each characterization technique a vital imperative.

2.5.1.1 Spectroscopy

Spectroscopy is a characterization technique used to study the interaction between matter and electromagnetic radiation often in the form of light. It measures how a material interacts with light over a range of wavelengths. Generally, a sample is illuminated by a range of wavelengths and the reflected or transmitted light from the sample is separated into individual wavelengths

and the intensity is measured. This can give information about the electronic and bonding structure of a material.

Transmission and reflection spectroscopy of thermochromic VO_2 in the ultraviolet (UV), visible (Vis) and infrared (IR) are used to measure the transmittance $T(\lambda)$ and reflectance change $R(\lambda)$ due to the transition from insulating VO_2(M) to metallic VO_2(R). Absorption $\alpha(\lambda)$ of the VO_2 at a given wavelength can be calculated from transmittance and reflectance.

$$\alpha(\lambda) = 1 - R(\lambda) - T(\lambda) \quad (1)$$

Typically, these measurements are conducted with light incident upon the sample at angles very close to perpendicular or normal incidence ($\theta \approx 0$). While VO_2 films don't have large optical changes in the visible spectrum [68], VO_2 films have been reported to exhibit up to a 50-70% transmittance difference upon transition from insulating to metallic between 2.5 μm and 10 μm as characterized by spectroscopy [26, 57, 69]. The optical switching amplitude can be correlated to the VO_2 film thickness, stoichiometry, dopants, and defects.

In the development of smart radiator designs incorporating thermochromic VO_2, the measurement of emittance of multilayer stack configurations is achieved using directional reflection spectroscopy. These configurations are referred to as variable emissive multilayers (VEMs). Given their application in radiative devices, it is essential to account for emissivity in all directions, not solely at normal incidence. The VEM designs discussed will be opaque so due to the conservation of energy and Kirchhoff's radiation law, $\alpha(\theta, \lambda) = \epsilon(\theta, \lambda)$, the directional

emissivity $\epsilon(\theta, \lambda)$ at a given wavelength and angle of incidence is calculated from the direction reflectance $R(\theta, \lambda)$.

$$\epsilon(\theta, \lambda) = 1 - R(\theta, \lambda) \tag{2}$$

The total hemispherical emittance at a given temperature is given by integrating the directional emissivity over the wavelength and angle range while normalizing to the black body spectrum with Planck's equation [70].

$$\epsilon(T) = 1 - \frac{\int_0^\infty R(\theta, \lambda) P(\theta, \lambda, T) d\lambda}{\int_0^\infty P(\theta, \lambda, T) d\lambda} \tag{3}$$

Planck's equation $P(\theta, \lambda)$, which expresses the limit of a perfect blackbody at a given temperature, is given by

$$P(\theta, \lambda) = \frac{2hc^2}{\lambda^5 (e^{hc/\lambda T k}) - 1} \tag{4}$$

where h is Planck's constant, c is the speed of light, T is the absolute temperature and k is the Boltzmann constant. Assuming symmetry along one angle, total hemispherical emittance can be calculated when the reflectance has been measured over a sufficiently wide range of incidence angles to permit integration over the hemisphere. Reflectance measurements out to 25μm are necessary for accurate calculation of emittance [71].

Measuring and understanding the spectral response of VO_2 is important not only to developing optimal synthesis techniques to achieve VO_2 with high transition amplitudes but for accurately measuring the total emittance of VEM designs upon which future device performance will rely.

2.5.1.2 Ellipsometry

Ellipsometry of VO_2 is used to evaluate the thickness and optical constants of the film. Ellipsometry measures the Psi (Ψ) and Delta (Δ) of the sample which describe the change in polarization that occurs when the measurement beam reflects off with the sample surface. The difference in the response of the sample to p and s-polarized light causes a change in the reflected polarization which is measured by the amplitude ratio ($tan\Psi$) and phase difference (Δ). This is displayed in Equation 5,

$$\frac{r_p}{r_s} = tan\Psi e^{i\Delta} \qquad (5)$$

where r_p and r_s represent the reflectivity of the p- and s-polarized light.

When fitting the ellipsometry data, an optical model is created using oscillators to model the dispersion. Frequently Gaussian oscillators are used in combination when modeling dielectric compounds and have provided accurate descriptions over a wide range of wavelengths for VO_2[26, 50, 72, 73] . Insulating VO_2(M) usually exhibits a refractive index (n) of between 2 to 3 and a decreasing extinction coefficient (k) less than 1 from 0.5μm to 10μm.

For metallic films, a Drude oscillator can be added to model the dispersion of free charge carriers in the material. Optical constants for VO_2 have been reported in several studies that cover UV/VIS and IR spectrum [26, 50]. Metallic VO_2(R) usually exhibit both an increasing refractive index (n) and extinction coefficient (k) from .5μm to 10μm.

Measuring optical constants and thickness of VO_2 is essential for building a model for how insulating and metallic VO_2 will behave in a VEM.

2.6 Fabry-Perot Multilayers

An ideal variable emissive radiator should exhibit high emissivity when at high temperatures and low emissivity when at cold temperatures. VO_2 films exhibit properties opposite to this behavior. By using a multilayer design utilizing a Fabry-Perot resonance cavity, the insulating and metallic properties of VO_2 can be harnessed into a multilayer with properties of an ideal variable emissive radiator.

A Fabry-Perot cavity is formed when two highly reflecting and parallel surfaces are separated by a lossless spacer material forming a resonant signal based on the spacer material thickness due to constructive interference [74]. Fabry-Perot interferometers are commonly used in a variety of applications to control and measure the wavelength of light [75]. Recently it has been demonstrated that a three-layer thin film multilayer utilizing a Fabry-Perot cavity can yield near perfection absorption peaks[76]. Based on the length d and refractive index n of the spacer material, the resonance wavelengths λ of high absorption will be created

$$\lambda = \frac{4nd_s}{j} \qquad (6)$$

at odd integers of j [77] . The Fabry-Perot resonance occurs when there is a 2π phase shift of the electric field inside the cavity forming a resonant standing wave which enhances the electromagnetic field at the interfacial region between the spacer and the top and bottom reflecting surfaces [76, 78]. The absorption of the light at the reflecting surface is proportional to the square of the electric field [79]. Using this effect, Fabry-Perot resonator cavities designs have been demonstrated to increase thermal emission and can be easily tuned by changing the cavity thickness [80] which make them ideal for use in variable emissive radiator designs utilizing VO_2.

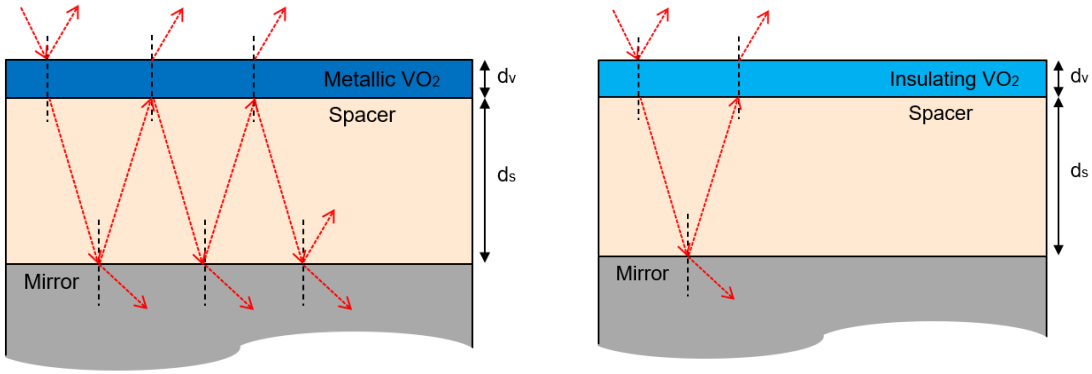

Figure 6: (Left) Metallic VO_2 top layer creating a Fabry-Perot resonance and high absorptive/emissive Multilayer (Right) Insulating VO_2 allowing transmission of light and a highly reflecting Multilayer.

When the radiator is at high temperature the VO_2 is reflective in its metallic state, producing a strong absorption and emission enhancement from the Fabry-Perot Cavity. At low temperatures, the VO_2 is insulating and transmissive letting the multilayer stack operate as a conventional enhanced mirror with a low emittance that is mostly dependent upon the underlying

mirror coating. The spacer layer thickness d_s will change where the resonance peaks occur as illustrated in Figure 7. The thickness of the VO_2 will change the strength and width of the resonance response and adjust the position as well [76-78]. This is illustrated in Figure 8.

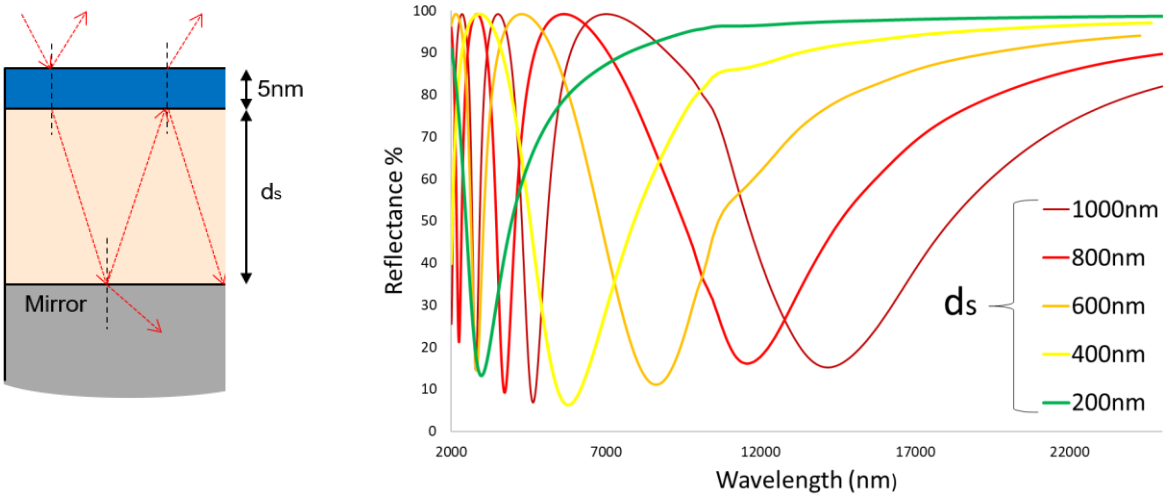

Figure 7: Example reflection curve of a VO_2 resonator modeling a silicon space (n=3.4) with a varying thickness

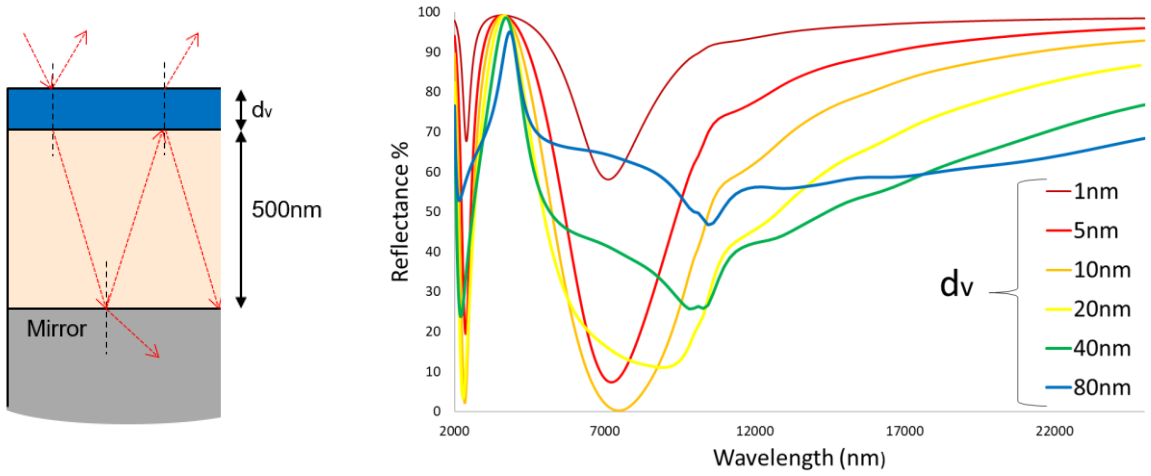

Figure 8: Example reflection curve of a VO_2 resonator modeling a 500nm Silicon space (n=3.4) with varying VO_2 thickness.

As outlined in Equation 6, the design of a VO_2 VEM can be tailored to achieve a Fabry-Perot resonance absorption at a designated wavelength. Referencing from the black-body spectra depicted in Figure 9, the optimization of the design choice is specifically aimed at maximizing emissivity in the hot VO_2 metallic state, with a focus on achieving maximal performance at a wavelength near 9 µm or 10 µm as it aligns to the peak spectral radiance of the black body curve which is related to the emittance of the multilayer via Equation 3.

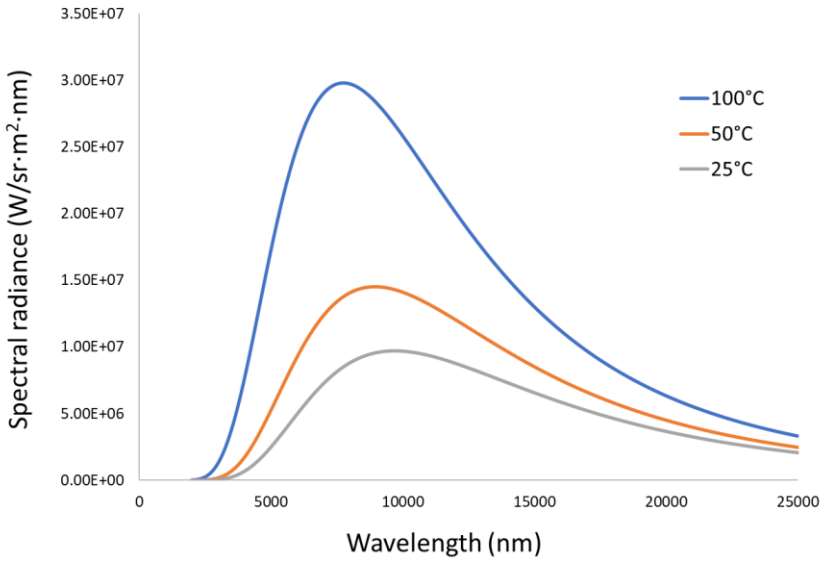

Figure 9: Black Body Spectral radiance spectra calculated at various temperatures.

The selection of the spacer material is a pivotal factor in VO_2 VEM design. Theoretical modeling has shown that reducing the refractive index of the spacer layer results in the broadening of the absorption range at elevated temperatures [81]. However, the spacer must exhibit excellent infrared (IR) transparency to ensure high IR reflectivity when in the low-temperature state. This, in turn, will generate the most significant change in emissivity, denoted

as $\Delta\epsilon$, from the low-temperature low-emissivity state ϵ_L to high-temperature high emissivity state ϵ_H, serving as the primary metric for an optimal VEM.

$$\Delta\epsilon = \epsilon_H(T_{high}) - \epsilon_L(T_{low}) \quad (7)$$

Reported VEM designs have ϵ_L ranging from 0.1 to 0.3 and ϵ_H to 0.4 and higher.

Table 1 presents various experimental demonstrations showcasing the exceptional performance of VO_2-based VEMs in terms of $\Delta\epsilon$. Hendaoui et al. achieved a hemispherical $\Delta\epsilon$ of 0.46 using a SiO_2 spacer layer in combination with undoped VO_2. When employing a tungsten-doped VO_2 layer, their $\Delta\epsilon$ was 0.43, and the critical transition temperature was 31.5°C [5]. It's worth noting that SiO_2 is constrained by its absorption peak in the 8-10μm range, as will become evident in presented results. Taylor et al. obtained a $\Delta\epsilon$ of 0.45 with the use of a silicon spacer [4].

Kim et al., employing a BaF_2 spacer, achieved a normal emittance of $\Delta\epsilon$ =0.49 and a hemispherical $\Delta\epsilon$ of 0.35. This highlights a noteworthy discrepancy between reported normal and hemispherical emittance values [6]. Normal emittance only takes into calculation the reflectance of the multilayer at normal incidence which leads to an overestimate of actual performance as it doesn't account of the angular dependence of the multilayer design. In the field, there appears to be a prevailing trend of reporting only normal $\Delta\epsilon$ values, despite the need for hemispherical data when calculating radiative power, primarily because the former tends to be significantly higher.

The most remarkable achievement in a straightforward three-layer VO_2-based VEM is reported by Beaini et al., who attained a normal incidence $\Delta\epsilon$ of 0.66 by employing a CaF_2 spacer [81]. This outcome is in line with expectations, given CaF_2's broadband infrared transparency and low refractive index.

The Fabry-Perot resonance multilayer stack design has demonstrated its suitability for VEMs, thanks to its straightforward and adjustable resonance structure. That same quality also renders it well-suited for optimization.

Table 1: Experimental VEM Results from 300K to 375K with different spacer Materials

Spacer	Hemispherical $\Delta\epsilon$	Near Normal $\Delta\epsilon$	Source
SiO_2	0.46	0.49	Hendaoui et al. [5] [82]
Si		0.45	Taylor et al. [4]
BaF_2	0.35	0.49	Kim et al. [6]
Al_2O_3		0.46	Kim et al. [83]
HfO_2		0.55	Wang et al. [84]
CaF_2		0.66	Beaini et al. [81]

2.7 Optimization and Enhancement of Fabry-Perot Design

The modeling of the Fabry-Perot resonance design proves highly advantageous for optimization due to its straightforward structure and the ease with which resonance can be adjusted, as previously discussed. These models are primarily geared towards optimizing the largest $\Delta\epsilon$ by manipulating spacer and VO_2 thickness to achieve the desired performance at both cold and hot temperatures, as outlined in Equations 2-4 and assessed through reflection calculations using the Transfer Matrix Method (TMM).

Notably, Zhang presented a noteworthy optimization of a VEM, employing either SiO_2 or Al_2O_3 spacer layers, which resulted in a normal incidence $\Delta\epsilon$ of 0.47 [85]. Additionally, Wu introduced an optimization strategy employing a BaF_2 spacer design, yielding a remarkable normal incidence $\Delta\epsilon$ of 0.64 [86].

Enhancement layers on top of the VO_2 have been studied for a variety of optical applications including increasing luminous transmittance [68] and enhanced emittance-switching [87]. Bragg mirror reflectors have been modeled on VO_2 Fabry-Perot cavity designs to minimize the solar absorption [88, 89], a requirement for future space radiators. Designs containing multiple layers of superposed VO_2 Fabry-Perot cavities have been simulated, and achieved normal $\Delta\epsilon = 0.78$ [19] but would be highly difficult to fabricate due to the need to deposit VO_2 at high temperatures. One of the most impressive experimentally proven designs in the field today is a thinned silicon substrate with a VO_2 Fabry-Perot cavities on one side and a 5-22μm antireflection coating on the other side, achieving a hemispherical $\Delta\epsilon = 0.62$ and a solar absorption less than 0.15 [90].

This study will propose an enhancement layer directly on top of a VO_2 in a Fabry-Perot cavity design which directly enhances the absorption of the VO_2 layer in the metallic state and thus the emissivity of the multilayer. Only one other study [91] has examined coatings as direct enhancements to a Fabry-Perot multilayer design, but to the author's knowledge the present work is the first known experimental synthesis and testing of this approach.

2.8 Electric Field-Induced Absorption in Multilayer Structures

To understand how this study's proposed enhancement layer will increase the absorption in the VO_2, it is necessary to review electric field theory through a multilayer stack from an optics perspective. Materials, made up of mostly stationary charged particles, interact with light entirely though the electric field. When the electric field amplitude is high, the potential for interaction with the material is great. When multilayer optical films are illuminated by light, standing wave patterns of the electric field form due to reflection at each interface. The standing wave patterns vary considerably due to the position and the wavelength of the light [79, 92].

The propagating electric field E' and magnetic field H' in a multilayer can be derived from the characteristic matrix shown in Equation 8 [92],

$$\begin{bmatrix} E' \\ H' \end{bmatrix} = \begin{bmatrix} cos\delta & \frac{isin\delta}{y} \\ iysin\delta & cos\delta \end{bmatrix} \begin{bmatrix} E \\ H \end{bmatrix} \tag{8}$$

with complex tangential amplitudes of the electric field E and magnetic field H and admittance y. For a thin absorbing layer of thickness d embedded in a multilayer, the phase term is

$$\delta = \frac{2\pi(\mathrm{n} - \mathrm{ik})\mathrm{d}}{\lambda} \tag{9}$$

and the input irradiance and exit irradiance through that film are given by

$$I_{in} = \frac{1}{2} Re(E' \cdot H'^{*}) \text{ and } I_{exit} = \frac{1}{2} Re(E \cdot H^{*}) \quad (10)$$

where * denotes the complex conjugate. The irradiance absorbed by the thin film is therefore given by the difference of the two and can be proven to be

$$I_{absorbed} = \frac{2\pi nkd}{\lambda} \cdot \Upsilon \mathcal{E}^2 \quad (11)$$

where Υ is the optical admittance and the normalized electric field intensity squared is

$$\mathcal{E}^2 = E \cdot E^{*} \quad (12)$$

From Equation 11, the magnitude of absorbed energy is directly proportion to the thickness d and extinction coefficient k of the film as well the electric field intensity in the film $\mathcal{E}^2$.

In the 3-layer VEM, the Fabry Perot design forms an enhanced electric field at a resonant wavelength. This enhanced electric field extends into the VO_2 layer thus increasing the absorption of the metallic VO_2 consistent with Equation 11. Improvements to this design are feasible if additional enhancement layers could be used to increase the electric field inside the metallic VO_2 layer at broadband wavelength. This would further increase the absorption of the metallic VO_2 and thus the $\Delta\epsilon$ of the VEM.

3.0 Experimental

VO_2 samples were synthesized, followed by structural and optical characterization, with the aim of determining their thermochromic properties, optical transition amplitude, and transition temperature. Additionally, VEM coatings were fabricated and subjected to optical testing to assess changes in emittance.

3.1 Sputtering

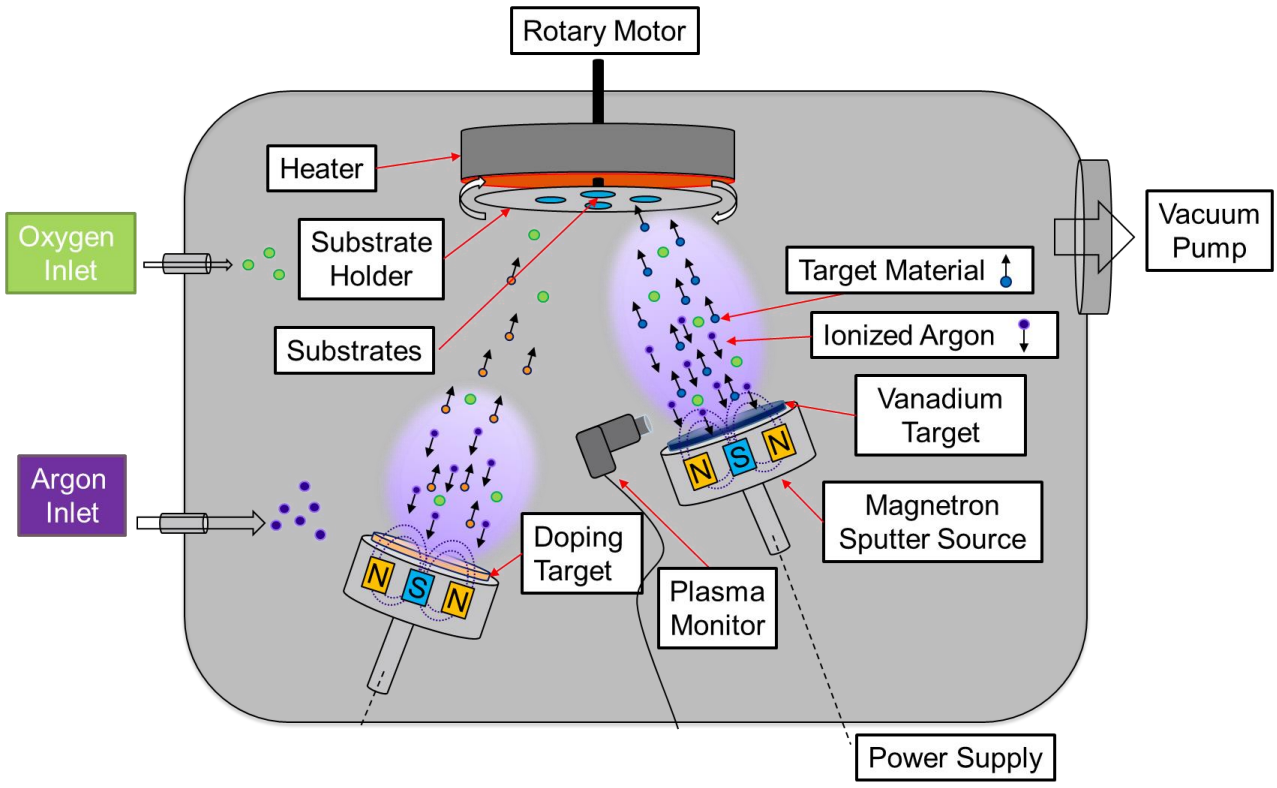

Figure 10: Diagram of the sputter chamber used to deposit VO_2. Vanadium is sputtered from the magnetron source on the right with the closer working distance. A plasma monitor records the spectra of the plasma and is used to control the flow rate of the oxygen and argon. The second Magnetron source on the left is used for co-sputtering to dope the VO_2 films.

VO_2 thin films were synthesized using radiofrequency (rf) magnetron sputtering in a vacuum chamber, which was evacuated to a base pressure below 1e-6 torr (1.3e-4 Pa). A

diagram of the sputter chamber is shown in Figure 10. A 3-inch (7.62cm) sputtering target composed of 99.9% pure vanadium was operated at 300 W, and the reflected power was carefully maintained near zero through an automatic capacitance tuning network. The Vanadium target was sputtered at a working distance of 12.5 cm from the substrate holder. Samples were deposited at a pressure of 2 millitorr (2mtorr) (0.267 Pa) with a constant flow rate of argon at 9 standard cubic centimeters per minute (sccm), along with a variable oxygen flow. The oxygen flow rate was regulated through a spectroscopic plasma monitoring system to maintain a consistent ratio between the intensity of argon at 772 nm and oxygen at 777 nm in the plasma emission spectra. Plasma spectra were captured at intervals of 100 milliseconds and subsequently fed into a PID controller responsible for managing the oxygen flow via a mass flow controller (MFC).

The substrate holder, located 0.25 inches (6.35mm) in front of the ceramic heater, was heated by a nickel-chrome radiative heater with a ceramic top plate capable of reaching a maximum temperature of 800°C. The substrate holder was electrically floating. To achieve the desired pre-deposition conditions, the front side of the substrate holder was monitored via a thermocouple and was gradually heated to reach 500°C. This required the radiative heater to reach an internal temperature of 790°C. The same conditions were then repeated during VO_2 deposition without the thermocouple so that the substrate plate could rotate freely.

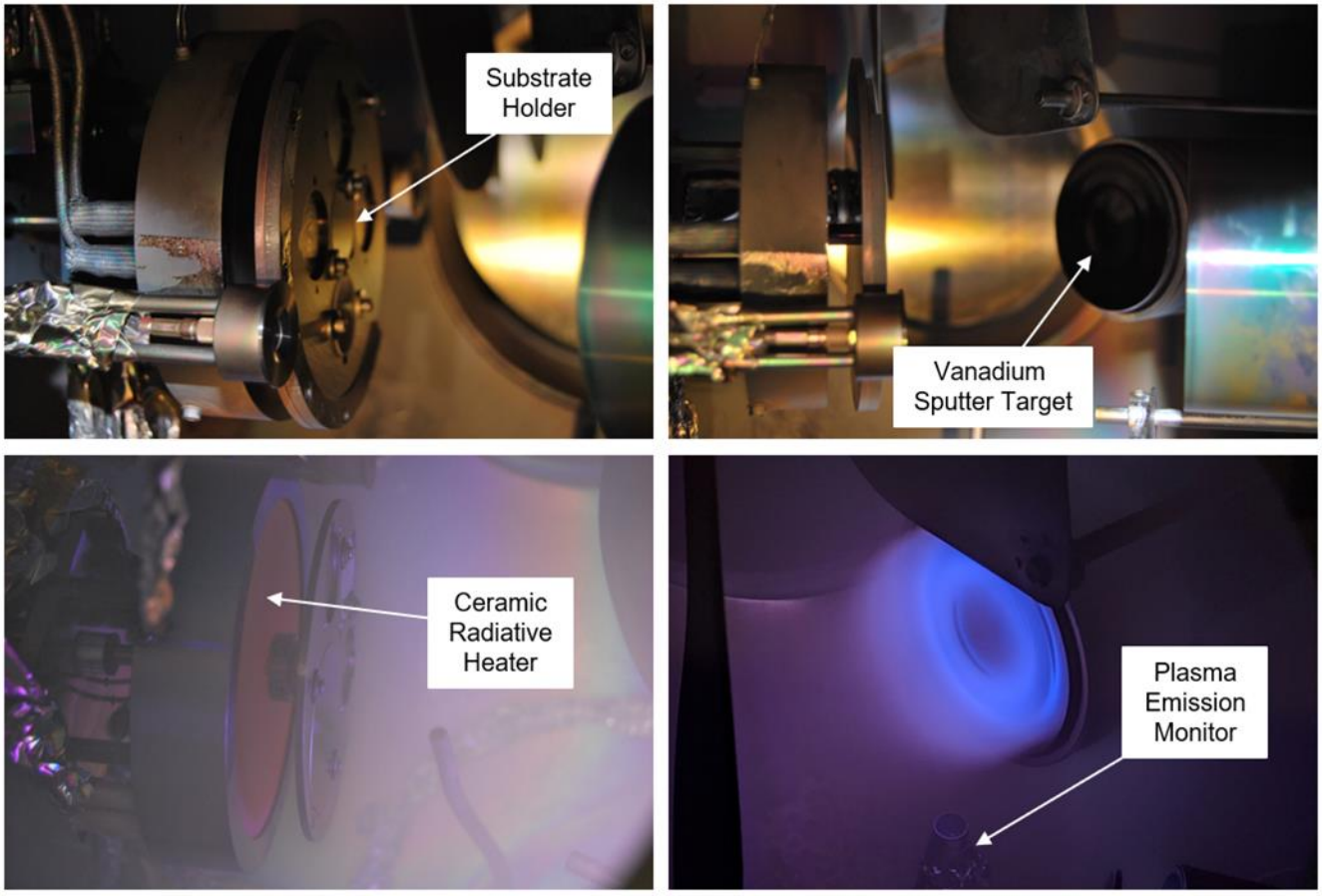

Figure 11: Photos of sputter chamber setup showing substrate holder, vanadium sputter target, ceramic radiative heater and the plasma emission monitor.

Doping of the VO_2 films was carried out by simultaneously co-sputtering a vanadium target and a tungsten, titanium, or molybdenum target. Tungsten was deposited at the lowest feasible power, 8 watts, while still maintaining a stable plasma. Titanium was sputtered at 250 W, and molybdenum was sputtered at 15 W.

For the VEM designs, the silver, silicon, and SiO_2 layers were deposited in a separate magnetron sputtering chamber before being transferred to the same chamber mentioned above for sputtering with VO_2, following the established procedure. A 50nm barrier layer of silicon nitride was experimentally determined to be essential between the silver and silicon layers to

preserve high reflectivity by preventing interatomic diffusion during substrate heating before the VO_2 deposition.

3.2 Structural Characterization

Crystal structure of the VO_2 examined by XRD was taken on a Rigaku SmartLab SE Diffractometer using copper Kα radiation (40kV, 30mA) and a HyPix-400 2D Detector. Scan were taken in Parallel beam mode with a 2° glancing angle and a 0.015° degree step size.

Relative elemental compositions of VO_2 films were analyzed by X-ray photoelectron spectroscopy (XPS). A PHI Versaprobe II Scanning XPS Microprobe (Physical Electronics, Chanhassen, MN, USA) with monochromatic aluminum K-alpha source (1.486 keV) was used with a beam spot size of 200 um. Hemispherical electron energy analyzer with a takeoff angle of 45° and a pass energy of 187.85 eV was used for obtaining survey spectra from which relative atomic percentages of elements were determined by quantitative peak fitting analysis. Before XPS scans were taken, samples were sputtered with Argon to remove the top 3nm of the film so surface species non-characteristic of the bulk film were removed.

Surface morphology and grain structure of VO_2 films were examined by scanning electron microscopy (SEM) observations. A JEOL JSM-7600F field emission scanning electron microscope was used in secondary electron imaging (SEI) mode and scans were taken at 50kx magnification.

3.3 Optical Characterization

The optical switching behavior of deposited VO_2 films on fused silica were determined by transmission spectroscopy using a Lambda 900 spectrometer (PerkinElmer) and a custom-

made heated sample holder. UV, VIS and NIR transmission spectra of 190nm to 2500nm wavelengths were measured at selected temperatures in the range of 25-90 °C. Hysteresis curves upon heating and cooling of the material were taken at 2500 nm with a ramp of 1°C/min.

The optical switching behavior of VO_2 films on double side polished silicon were determined by FTIR spectroscopy using a Perkin Elmer Frontier Optica and a custom-made heated sample holder. Measurements were taken from 2.5μm to 25μm.

Spectroscopy ellipsometry was measured on a VASE ellipsometer at Aerospace Corporation and both a RC2 Model and IR-VASE Ellipsometer (J.A. Woollam) at J.A. Woollam. The measurements on the VASE and RC2 Ellipsometer were taken from 0.193um to 2.5um at incident angles $55°, 60°, 65°, 70°, 75°$ and at 1nm intervals. Measurements were taken using the IR-VASE from 1.25μm to 34μm at incident angles $55°, 65°, 75°$. Ellipsometry was carried out at two temperatures: 30°C (VO_2 in insulating phase) and 100°C (VO_2 in metallic phase). Thickness and optical constants were evaluated by using the WVASE software. When fitting the ellipsometry data, gaussian oscillators were used to model the dispersion relationship in both the insulating phase and metallic phase. An additional Drude oscillator was added in the metallic phase. Thickness values were used to calibrate the growth rate of the VO_2, and optical constants were used to model and optimize VEM designs.

IR reflection spectra of VEM designs were measured on a Surface Optics SOC-100 hemispherical direction reflectometer (HDR) coupled to a Nicolet i550 FTIR spectrometer (Thermofisher). Samples were mounted on a heating stage. The SOC-100 HDR uses a 2π imaging hemiellipsoid to diffusely illuminate the sample using a 700°C blackbody. The source radiation is chopped between source and sample so that self-emission signal background is eliminated. A pick off mirror directs reflected light from the sample at varied angles to the

spectrometer. Reflection calibration is made by comparing the sample to a standard of known directional reflectance. The sample and standard are moved in and out of the pickoff mirror path at every angle. Reflection measurements were taken at 11°, 20°, 30°, 40°, 50° and 60° degree angles. Total hemispherical emissivity data was calculated using OMNIC Specta software. Reflection spectra was compared to modeled VEM spectra in the goal of achieving improved emittance switching $\Delta\epsilon$.

3.4 Optimization and Modeling

The modeling of VEM coatings was carried out using thin film optical modeling software TFCalc and MATLAB. The optical constants for VO_2 were determined through experimental ellipsometry, while those for silicon [93], barium fluoride [94], and silver [95] were sourced from existing literature.

The optimization of the emissivity change ($\Delta\varepsilon$) in a VEM was carried out using a custom-built genetic optimizer [96, 97] and gradient descent [98] function in MATLAB. Commercial thin film software is not capable of optimizing the performance thin film structures containing phase change materials with distinct optimization objectives for each state, such as achieving both high and low emissivity. The MATLAB optimizer was constrained to assign thick silver as the first layer and VO_2 as the third layer, but it had the freedom to select various materials for the intermediate spacer and to place materials on top of the VO_2 layer in order to maximize the emissivity transition. Emissivity values were derived from Equations 2-4 and assessed through reflectivity calculations using the Transfer Matrix Method (TMM).

Following a predefined number of genetic optimization rounds, the multilayer design was then subjected to a gradient descent optimizer. This optimizer adjusted the thickness of each

layer to further enhance the emissivity transition. Importantly, a thickness penalty was applied to the gradient descent optimizer to ensure that the design could be realistically fabricated.

4.0 Results and Discussion

4.1 Sputtering

A substantial portion of this project was dedicated to optimizing deposition conditions for the consistent deposition of a single-phase VO_2(M). However, this portion of the effort will be briefly mentioned rather than discussed in detail, as it is comparatively less novel than the results presented throughout the bulk of this section.

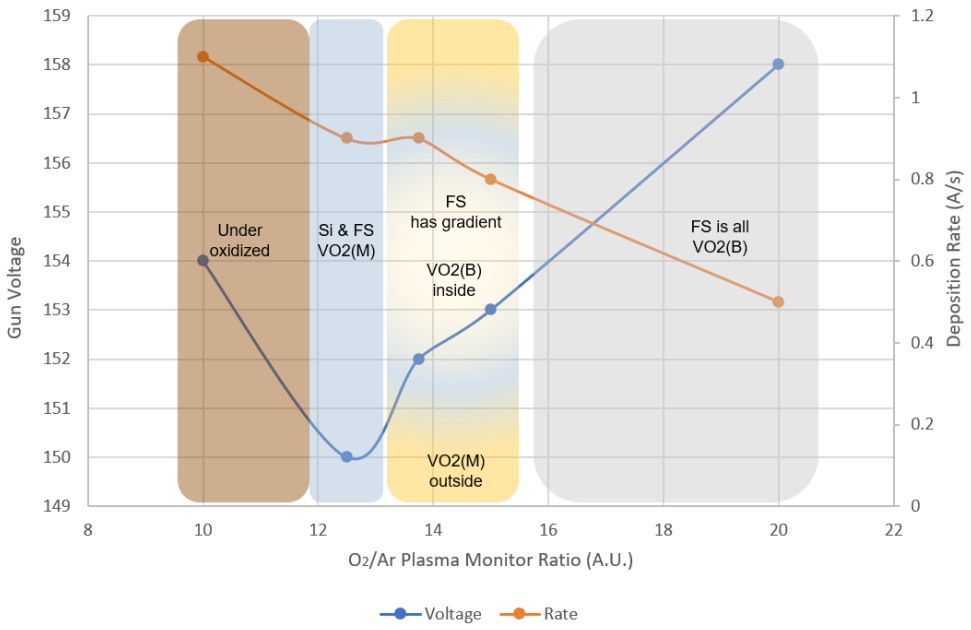

Figure 12: Diagram depicting the effect of the oxygen/argon ratio measured through a plasma emission monitoring system on the crystal structure of the deposited VO_2(M) and gun voltage and deposition rate during the sputtering process. Thermochromic VO_2(M) was observed in a precise gas ratio regime.

Highly oriented single phase VO_2(M) films were found to be repeatably deposited on both silicon (Si) and fused silica (FS) substrates in a narrow O_2/Ar working gas ratio regime, as illustrated in Figure 12. This window corresponded to an oxygen flow of 1.1 to 1.3sccm or 10-13% of the total flow. Of note is that the voltage of the plasma decreases below the VO_2(M) window and then increases as oxygen is increased. This is related to both the gas composition of the plasma and formation of an oxide film on the vanadium target [99]. The VO_2(M) window is also in the range where the vanadium target is starting to poison as evident by the decrease in deposition rate [60]. Above this oxygen window ratio, deposited films displayed gradients of VO_2(M) and VO_2(B) or were completely VO_2(B) as characterized by XRD.

4.2 Surface Morphology and Crystal Structure

After a O_2/Ar working regime had been achieved to repeatably achieve thermochromic VO_2, films were deposited with and without doping on a variety of substrates at similar thicknesses to understand the effects substrate material and doping would have on surface morphology, crystal structure and optical transition quality. All of this was down with the goal of achieving quality thermochromic VO_2 films in a VEM design. Table 2 provides an example of the VO_2 films deposited in this study.

Table 2: VO_2 depositions at varied thickness and doping on a variety of substrates

Sample	Thickness	Substrate 1	Substrate 2	Doping
Film 1	65nm	Silicon	Fused Silica	Undoped
Film 2	60nm	Silicon	α-Si Spacer	Undoped
Film 3	60nm	Silicon	α-Si Spacer	1.2 at.% Mo

SEM scans of a VO_2 Film 1 deposited on a silicon substrate display dense and close packed structure with an average grain size of 50nm (Figure 13). For magnetron sputtered films, this grain size has been related to high transition amplitudes [65].

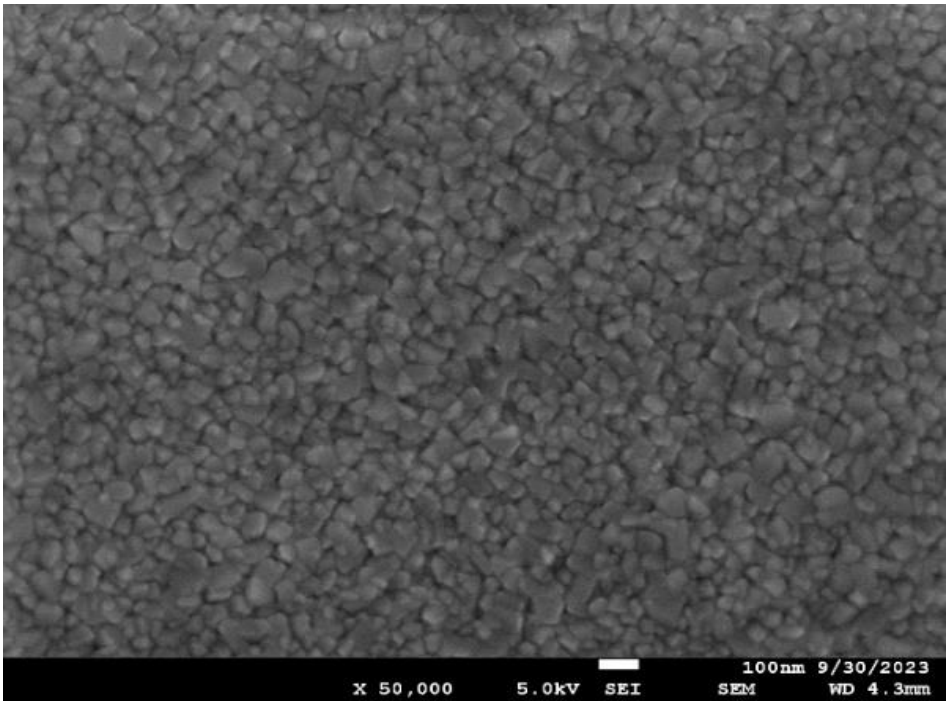

Figure 13*:* 50kx SEM scan of VO_2 deposited on Si Substrate. An average grain size of 50nm was calculated from the image.

An average grain size of 50nm was also achieved for VO_2 Film 2 simultaneously sputtered on to a silicon substrate and an a-Si sputtered spacer layer as part of a VEM (Figure 14, A & B). It can be interpreted that the grain size is likely thickness and process dependent and independent of the substrate difference between <100> oriented Si wafer and a-Si sputtered film. VO_2 Film 3 with 1.2% Molybdenum doping simultaneously sputtered on a silicon substrate and sputtered a-Si spacer layer also displayed an average grain size of 50nm (Figure 14, C & D). The molybdenum doping does not have an observable structural effect on the grain size or compactness of the film.

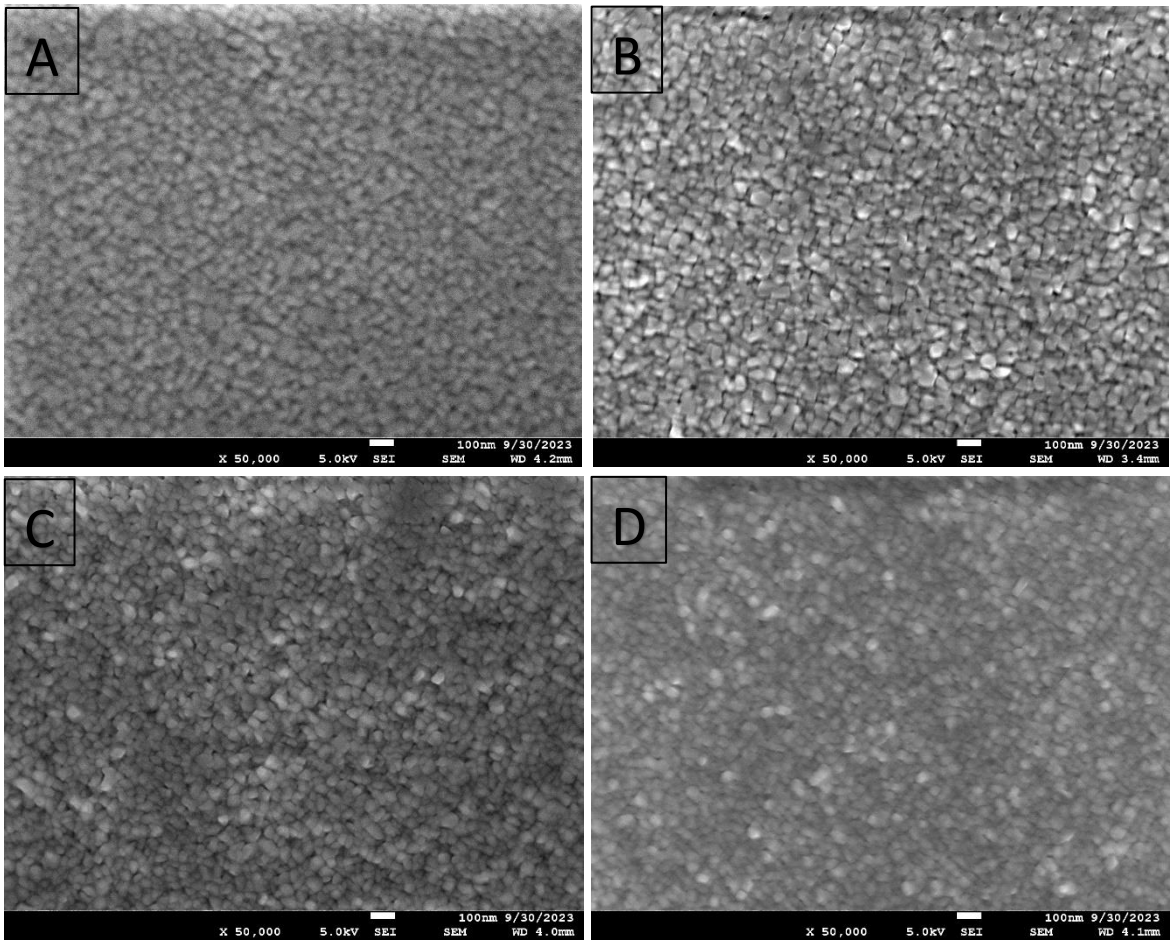

Figure 14: 50kx SEM scan of A) VO_2 on Si B) VO_2 on α-Si Spacer C) $V_{1-x}W_xO_2$ films on Si D) $V_{1-x}W_xO_2$ films on a-Si Spacer. An average grain size of 50nm was calculated for all VO_2 films.

As illustrated in Figure 15, the X-ray diffraction (XRD) scans of VO_2 Film 1 deposited on both fused silica and silicon substrate reveal a well-defined crystal structure with a prominent peak at 27.9°, corresponding to the (011) plane of VO_2(M). This observation is consistent with previous research findings [49, 53]. Additionally, all other peaks observed in the XRD patterns correspond with the VO_2(M) phase, confirming the phase purity of the films.

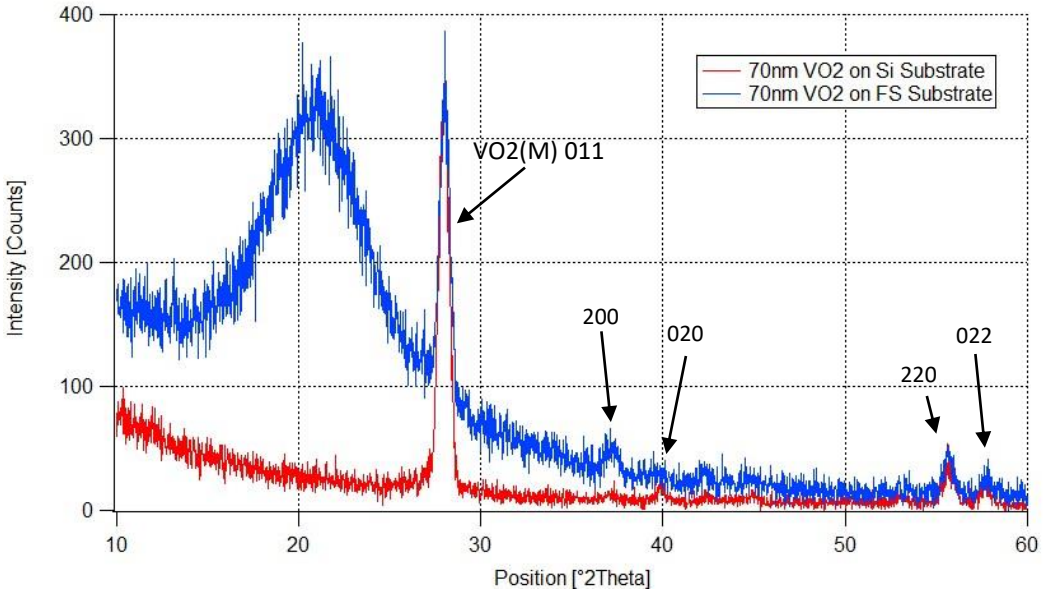

Figure 15: XRD patterns from VO_2 film deposited on silicon and fused Silicon substrates at 500°C with thickness of 70nm. All peaks correspond to VO_2(M).

The structural transition of VO_2 Film 1 on a silicon substrate from the insulating to metallic between 65 °C to 75 °C is depicted in Figure 16. The VO_2 monoclinic lattice (011) at 27.9° peak

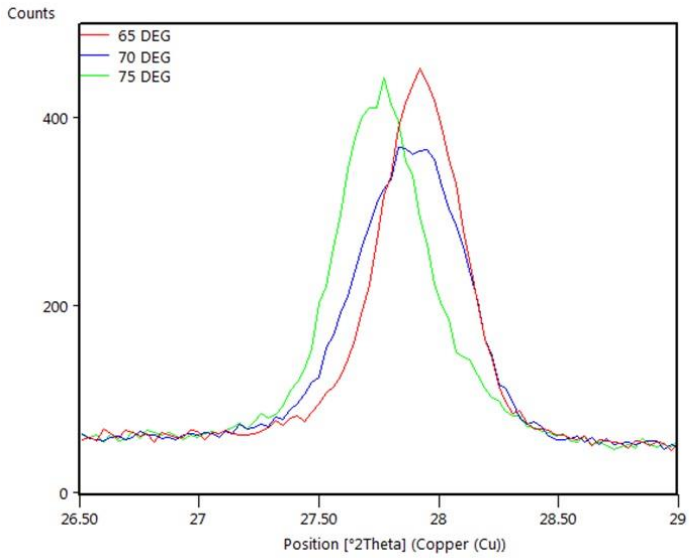

Figure 16: XRD patterns of VO_2 Film 1 taken at 65°C, 70°C and 75°C. The Peak transition from 27.9° to 27.6° shows a transition from (011) VO_2(M) to (110) VO_2(R) respectively.

transitions to the VO_2 rutile lattice (110) peak at 27.6°. This confirms the VO_2 film is undergoing a structural transition. After the films were structurally characterized and confirmed to be thermochromic VO_2(M) and to behave similarly across varied substates, the optical properties of the VO_2 were studied.

4.3 Optical Properties

The optical properties of VO_2 films were investigated with the aim of evaluating their suitability in a VEM design. Transmittance changes were measured to determine the transition amplitude, a critical parameter that needs to be maximized for effective VEM use. Additionally, the transition temperature and hysteresis were measured to gain insights into when the films would undergo a complete optical transition, transitioning from an insulating to a metallic state and back.

As depicted in Figure 17 (left), VO_2 Film 1 on FS, exhibits a substantial decrease in transmittance in the near-infrared (NIR) range when the VO_2 film transitions from cold insulating to hot metallic. Film 1 displays a transition ratio change of 83%, transitioning from 70% transmittance to 12% transmittance at 2500nm. In Figure 17 (right), the same VO_2 film is characterized by an optical transition midpoint at 64°C and a hysteresis width of 10°C. This information provides important characterization of the material's optical behavior during its transition from the insulating to the metallic state and vice versa.

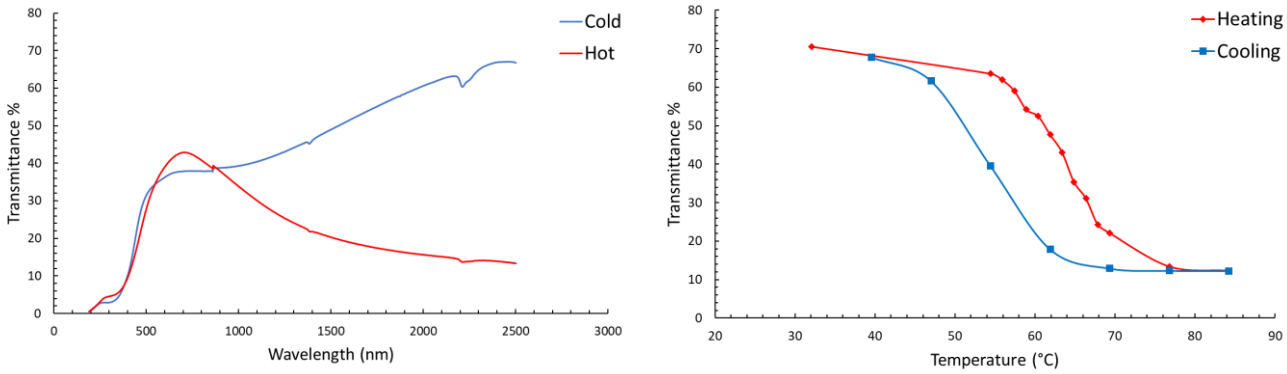

Figure 17: (Left) UV/VIS/NIR transmission spectrum of VO_2 on FS substrate in insulating (Cold) and metallic state (Hot). (Right) Hysteresis of VO_2 transmittance at 2500nm on FS substrate upon heating and cooling

VO_2 Film 1, when sputtered onto a silicon substrate, exhibits a substantial 80% transition ratio change in transmittance 5µm, as demonstrated in Figure 18. The drop in the transmittance with increased wavelength as well as the large spectral features are due to the silicon substrate [93]. This remarkable ability to switch in the infrared (IR) region affirms the potential suitability of this VO_2 material for use in a Fabry-Perot cavity VEM design.

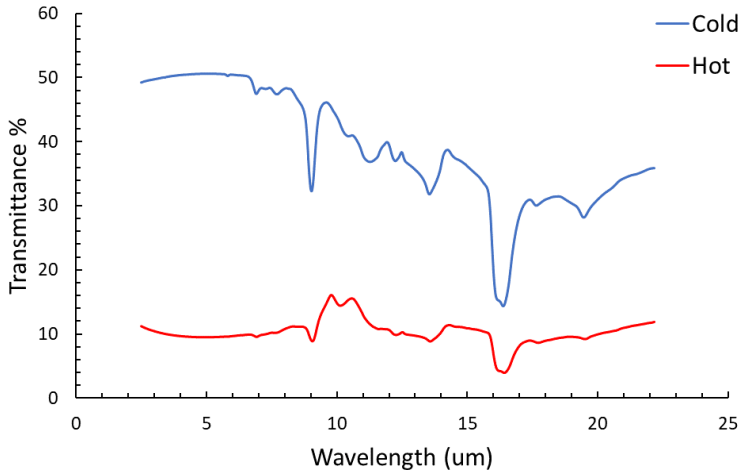

Figure 18: FTIR transmission of VO_2 sample on silicon in insulating (Cold) and metallic state (Hot). Spectral features are largely due to absorption bands in the silicon substrate.

Refractive indices of VO_2 extracted from ellipsometry spectra in both the UV/Vis/NIR and IR are presented in Figure 19 & 20. Film 1 and 2 (both VO_2 on Si substrate) were both measured in the cold insulating state at 25°C and in the hot metallic state at 100°C to ensure complete phase transition. This data was fitted together in WVASE software (J.A. Woollam) to an optical model consisting of a single side polished silicon substrate, native oxide and VO_2 layer. Thickness (t), refractive index (n) and the extinction coefficient (k) of the VO_2 films were evaluated from the model. Film 1 and Film 2 were fit with thicknesses of 65nm and 60nm respectively. The optical constants of Film 1 and Film 2 are nearly identical and play a crucial role in explaining why the reflection, absorption and thus transmission of the VO_2 film changes when transitioning from the insulating to metallic state. The optical constants obtained in this study are in good agreement with previous research on VO_2 films[6, 50]. This consistency underscores the importance of the design of the VEM and confirms that the VO_2 films used in the study are of consistent and regular quality.

Past the 2.5µm wavelength, the refractive index (n) and extinction coefficient (k) both increase with wavelength as the VO_2 films turns metallic. This is characteristic of a metallic film. The refractive index (n) and extinction coefficient (k) of the 25°C insulating film have significant IR features at 17, 20 and 25µm. These have been associated to the strong vibrational resonances from oxygen atoms in the VO_2 film[100]. These absorption peaks in (k) are likely to show up in VEM when an enhancement layer is applied.

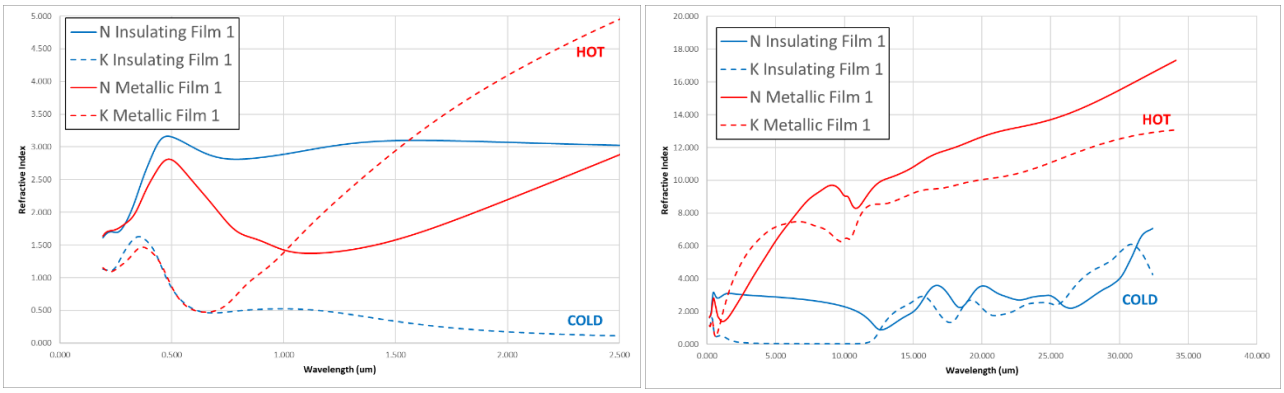

Figure 19: Extracted refractive indices of VO_2 Film 1 in (Left) UV/Vis/NIR (Right) IR

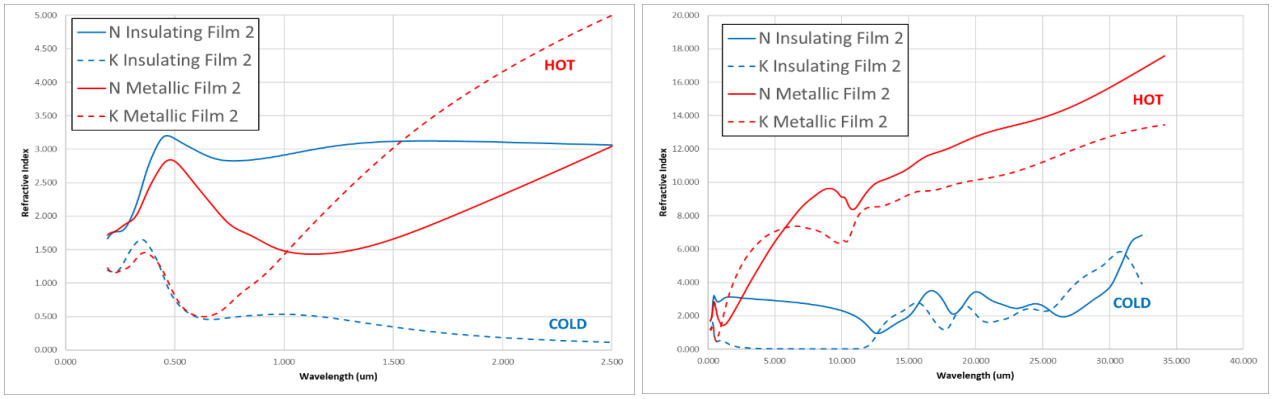

Figure 20: Extracted refractive indices of VO_2 Film 2 in (Left) UV/Vis/NIR (Right) IR

4.4 Doping of Vanadium Oxide Films

Ideal VEM designs will likely require lower transition temperatures to maintain stable temperatures for a variety of applications. Doping was studied with the goal of lowering the transition temperature deposited VO_2 closer to 30°C while considering the dopants effect on transition amplitude and hysteresis.

VO_2(M) doped films were deposited on Fused Silica by the co-sputtering of vanadium with either tungsten, titanium, or molybdenum. Results of the XPS scans of the of the doped VO_2 are presented in Table 3.

Table 3: Atomic Percentages in VO_2 film calculated from XPS

Sample	V	O	W	Ti	Mo	Ar
70nm VO_2 Tungsten Doped	33.2	65.1	1.1			0.6
70nm VO_2 Titanium Doped	31.6	65.3		2.2		0.9
40nm VO_2 Molybdenum Doped	33.6	63.7			1.2	1.5

The inclusion of 1.1 at% of tungsten atoms within the VO_2 film caused a reduction in the transition temperature, falling below the measurable range of the transmission measurement system, as depicted in Figure 21 (A). This suggests that the dopant effect exhibited by this film exceeds the 23°C/at% reported in other sources [49].

Introduction of 2.2 at% of titanium into the VO_2 film resulted in increased transition temperature to 68°C and a decrease of the hysteresis width. This agrees with previous studies [101, 102]. Reduction of the hysteresis width is advantageous for increasing the sensitivity of the optical response to temperature.

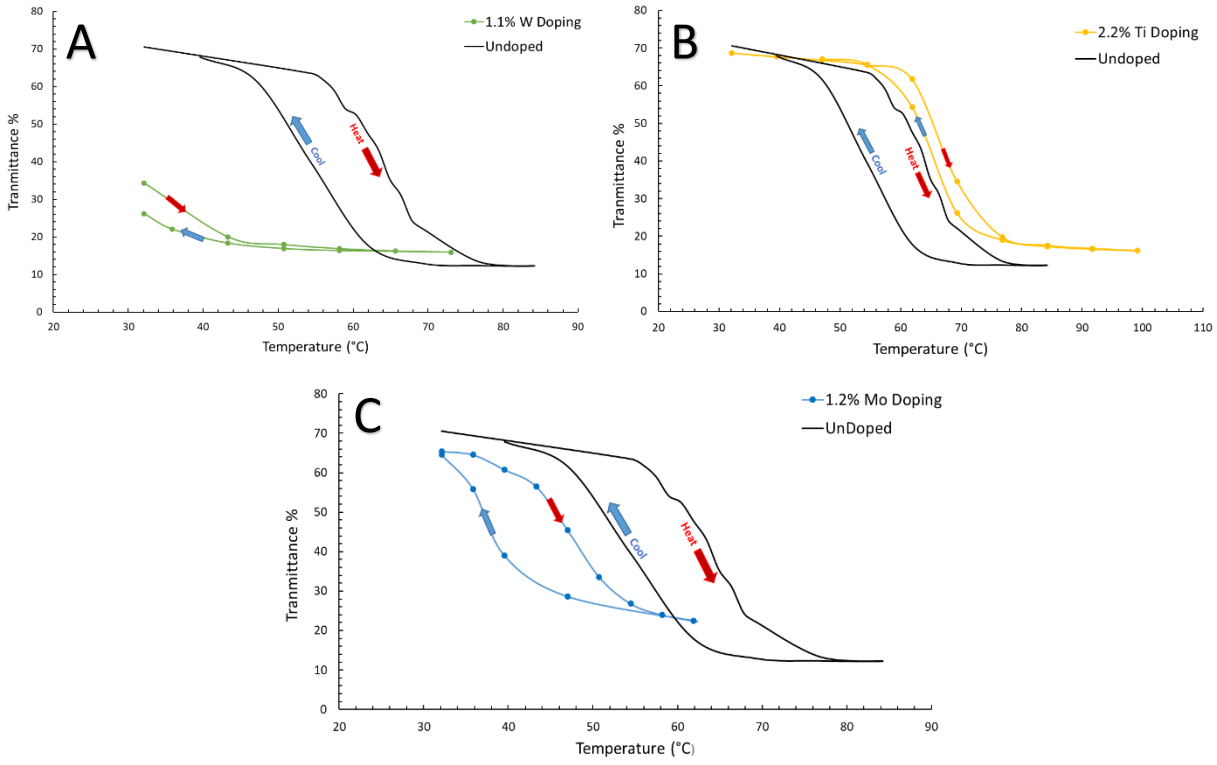

Figure 21: Temperature Dependent Transmission Spectroscopy at 2.5um of VO_2 films with A) 1.1at% tungsten doping B) 2.2at% titanium doping C) 1.2at% molybdenum doping

The introduction of 1.2% molybdenum doped films decreased the transition temperature to 48°C. The decrease in transition temperature effect of 13.3°C/at% molybdenum is comparable to previous studies[62, 63]. The hysteresis width is unaffected by the doping.

Because the doping effects of molybdenum was successfully measured, it was chosen instead of tungsten to be employed in creating a VEM with a lower transition temperature. The benefits of titanium doping are evident as well. Titanium doping can enhance VO_2 film sensitivity to temperature, and it holds potential for incorporation into future VEM designs, possibly in conjunction with molybdenum as a co-dopant.

4.5 Fabricated Variable Emissive Multilayers (VEMs)

Variable Emissive Multilayer (VEM) designs that integrate VO_2 can achieve both low emissivity at low temperatures and high emissivity at high temperatures. This study's objective was to construct several of these designs, varying VO_2 film thickness and spacer materials, with the aim of maximizing $\Delta\epsilon$ (the change in emissivity) and evaluating the alignment between the experimental results and theoretical models.

Silicon dioxide (SiO_2) was the first spacer layer in a VEM experimentally explored in this study. VO_2 thicknesses of 45nm, 60nm and 80nm were sputtered on top of 1000nm SiO_2 spacer and 200nm silver reflector, to study the effect of the VO_2 thickness in the VEM design and compare it to the Fabry-Perot resonance theory. Mid-wave-infrared (MWIR) reflectance spectra measurements of the multilayers at 30°C and 100°C as well as the calculated hemispherical emittance change are displayed in Figure 22.

As illustrated in Figure 22, in the cold (30°C) insulating and transparent state of the VO_2, all the multilayers act as IR reflectors except in the prominent absorption bands of SiO_2 near 10, 12 and 22µm [103]. Another absorption feature at 17µm appears to increase with the thickness of the VO_2 and can be correlated to the VO_2 absorption feature seen in the ellipsometry studies. At 100°C the VO_2 is metallic and the multilayer exhibits low reflectance due to the high absorption of the VEM due to Fabry-Perot resonant cavity. The hemispherical emittance change ($\Delta\epsilon$) has been computed for each design and is presented in Figure 22. The highest emittance change observed is 0.48 for a 45nm VO_2 topping layer, while the lowest emittance change is 0.28 for an 80nm VO_2 topping layer.

The increase in VO_2 thickness from 45nm to 80nm leads to a noticeable enhancement in the reflection spectrum when the VO_2 is in its metallic state. This alteration directly influences the computed hemispherical emittance, which is observed to decrease as the VO_2 thickness increases. This phenomenon aligns with the principles of the Fabry-Perot theory and the models discussed in Section 2.6.

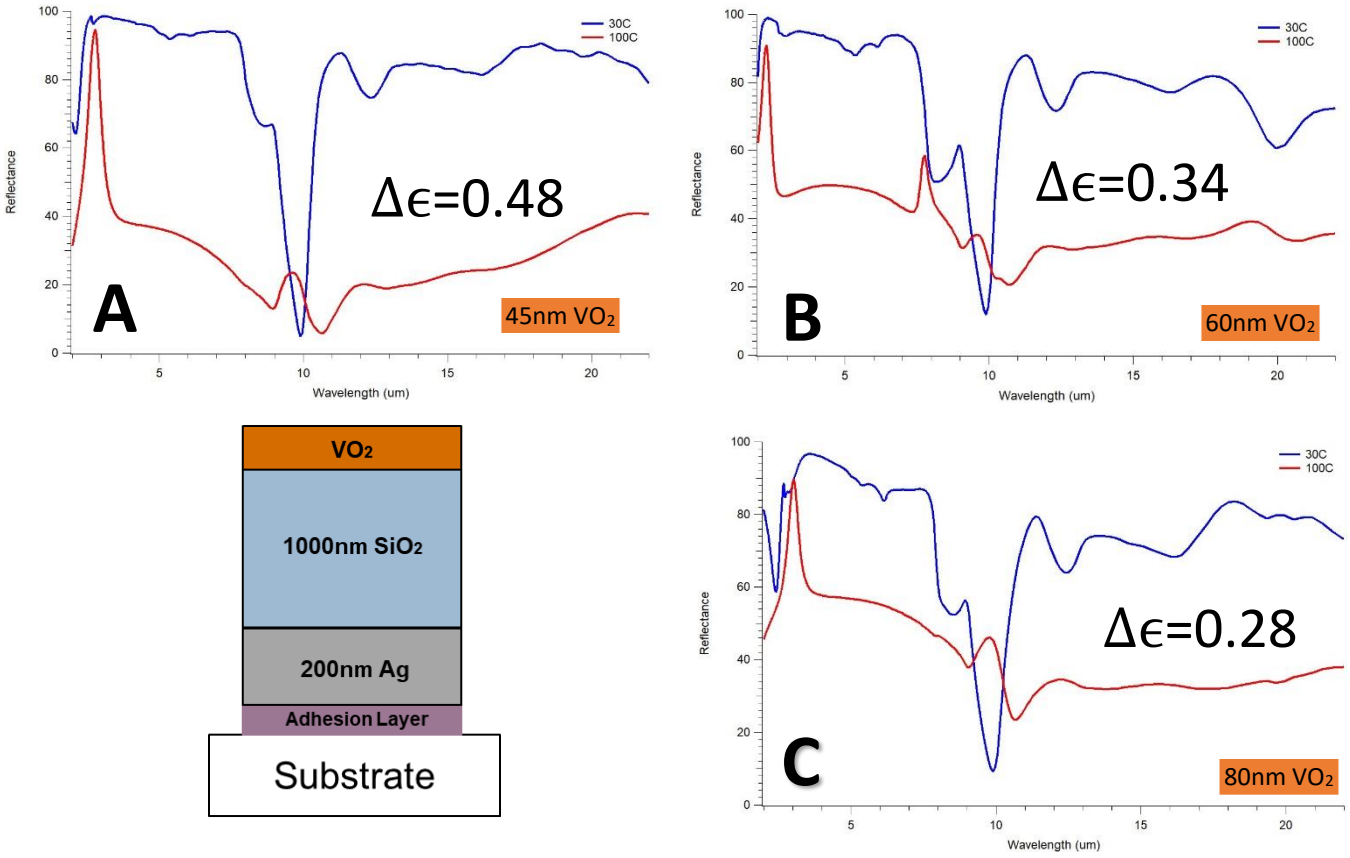

Figure 22: Diagram of Variable Emissive Multilayer composed of a silver bottom reflector, SiO_2 spacer and a topping VO_2 with varying thickness of VO_2 layer. Reflectance spectra of VO_2 with varying thicknesses of (A) 45nm (B) 60nm (C) 80nm. Measurements were taken at 30°C and the 100°C.The change in total hemispherical emittance from 300K to 375K is reported on the graph for each sample.

As shown in Figure 22A, the hemispherical $\Delta\epsilon$ achieved for the 1000nm SiO2 spacer and 45nm VO_2 is 0.48. When only the near normal incidence reflection curves of this VEM are considered for the calculation of emittance change, a normal $\Delta\epsilon = 0.54$ is achieved with a $\epsilon_L = 0.22$ at 30°C and $\epsilon_H = 0.76$ at 100°C. The discrepancy between the normal and hemispherical emittance $\Delta\epsilon$ demonstrates how reporting normal incidence leads to an overestimation of actual performance, which is directly related to hemispherical $\Delta\epsilon$, as it doesn't account for angular dependence of the multilayer design.

VEMs employing SiO_2 as a spacer layer face limitations in achieving the lowest possible emissivity in the cold state ($\epsilon_L \sim 0.2$) due to the absorption of SiO_2 in the infrared (IR) region. Because of this the maximal attainable $\Delta\epsilon$ is constrained. A spacer layer is proposed, featuring negligible absorption characteristics in the infrared (IR), specifically silicon.

Thin amorphous silicon does not have any prominent absorption bands in the 5-25μm IR region and so was experimentally studied in the second round of VEM devices. Using thin film design software (TFCalc), a thin multilayer stack design was optimized to achieve a low reflectance with a broad Fabry-Perot resonance peak at 9μm when VO_2 is the metallic state. Initial experiments failed due to diffusion reactions between the silicon spacer and bottom silver reflector during the heated VO_2 deposition. The design was then modified to feature a silicon nitride barrier layer placed between the sputtered silver and sputtered a-Si. Subsequent experiments proved that silicon nitride is an effective diffusion barrier between silicon and silver at temperatures required for depositing VO_2(M) [104].

The optimized design was calculated to achieve a normal $\Delta\epsilon$ value of 0.55 with a 200nm silver reflector, a 50nm silicon nitride barrier layer, a 500nm silicon spacer layer and a 25nm VO_2 topping layer. Optical constants for the VO_2 were modeled from the experimentally

deposited 60nm VO_2 presented in section 4.3. The VEM was fabricated to achieve this design and experimental MWIR reflectance spectra was taken and compared to the model as illustrated in Figure 23. The normal $\Delta\epsilon$ of the fabricated VEM was measured to be 0.44, significantly less than the modeled value of 0.55.

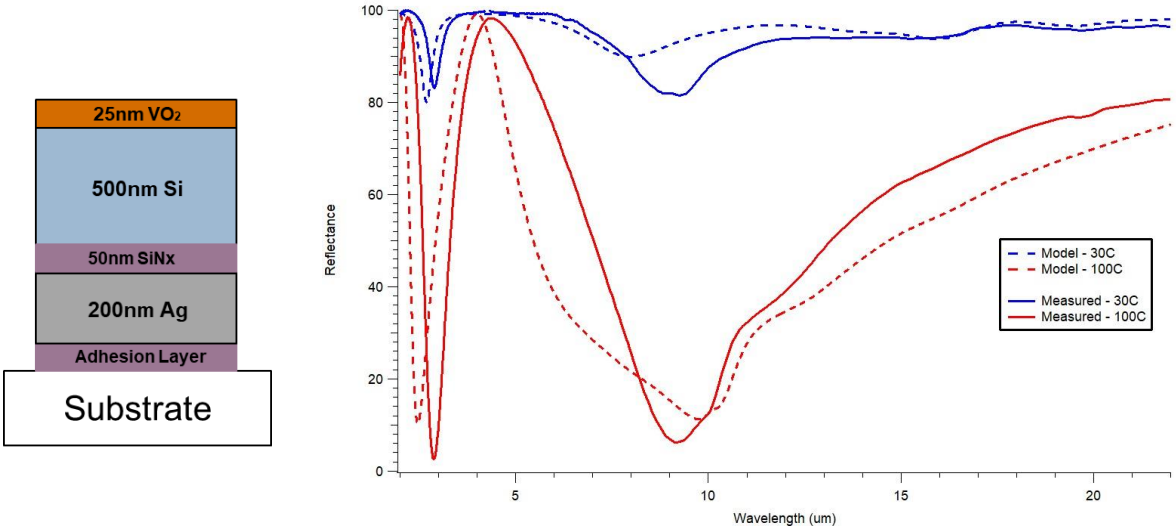

Figure 23: (Left) Diagram of radiator stack (Right) Modeled and Experimental reflectance spectra of 25nm VO_2 on a 500nm Si spacer VED at cold (30°C) and hot (100°C). Reflectance modeled in TF calc is also plotted.

To investigate the disparity between the experimental and modeled $\Delta\epsilon$ values, consider Figure 23. When examining the reflectance spectrum from the left side, note that the experimental quarter-wavelength interference peak at approximately 3 µm is shifted compared to the simulated peak at 2.65 µm. This observation leads to the conclusion that the experimental silicon spacer thickness is closer to 600nm, which is larger than the targeted 500nm silicon spacer as modeled in Figure 23. However, updating the model to incorporate a 600nm spacer

only results in a marginal decrease in the normal $\Delta\epsilon$ to 0.54, indicating that the spacer thickness is not the primary cause of the deviation.

At a temperature of 30°C, both the modeled and experimental VEM exhibit an absorption feature near 8 μm to 9 μm respectively. However, the experimental VEM absorption at 9um is significantly larger and thus an impact on the device's ability to achieve its optimized $\Delta\epsilon$. In the modeling software TFcalc, this absorption feature appears with and without the presence of a VO_2 or silicon nitride layer. The feature also moves with adjusted silicon thickness so it has been determined to be a very weak Fabry-Perot resonance following Equation 6, as the interface between silicon and air ($n = 1$) serves as a weak top reflector [78]. In the experimental data, the prominent absorption feature at 9 μm manifests in reflection measurements of the silicon spacer on a silver reflector even prior to the application of VO_2. This occurrence suggests a plausible connection to the presence of oxygen within or on the amorphous silicon layer.

At 100°C in Figure 23, the experimental results reveal a decrease in reflectance associated with the Fabry-Perot resonance peak at 9 μm. However, the observed resonance width in the experimental VEM is narrower than what was expected from the model. The most substantial factor contributing to the disparity between the modeled and experimental $\Delta\epsilon$ value is this difference in resonance width. This mismatch can be attributed to a variation in optical constants between the 25nm metallic VO_2 used in the experiment and the modeled VO_2, which relied on optical constants obtained from ellipsometry performed on a 60nm VO_2 sample. Unfortunately, the optical constants of a 60nm VO_2 film do not accurately represent the optical constants of a 25nm thickness due to structural defects, film stress, and strain as discussed in Section 2.3. Recognizing the constraints within the models and optimization of this study is essential for advancing the development of VEMs with maximized $\Delta\epsilon$.

Next the transition temperature of silicon spacer VEM with a 60nm VO_2 topping layer with and without 1.2at% Mo doping was studied with goal of lowering the transition temperature of the doped VEM while comparing the $\Delta\epsilon$ to the undoped VEM.

The undoped VO_2 displayed a transition temperature between 60°C and 65°C as illustrated in Figure 24. This is matching the transition temperature of previous 60nm VO_2 deposited on fused silica and silicon. The measured experimental normal $\Delta\epsilon$ is 0.43. Unlike the previously discussed VEM, this is comparable to the modeled value of $\Delta\epsilon = 0.41$. The model better represents the experimental data in this VEM design because optical constants of the modeled 60nm VO_2 are more accurate to the experimental 60nm VO_2.

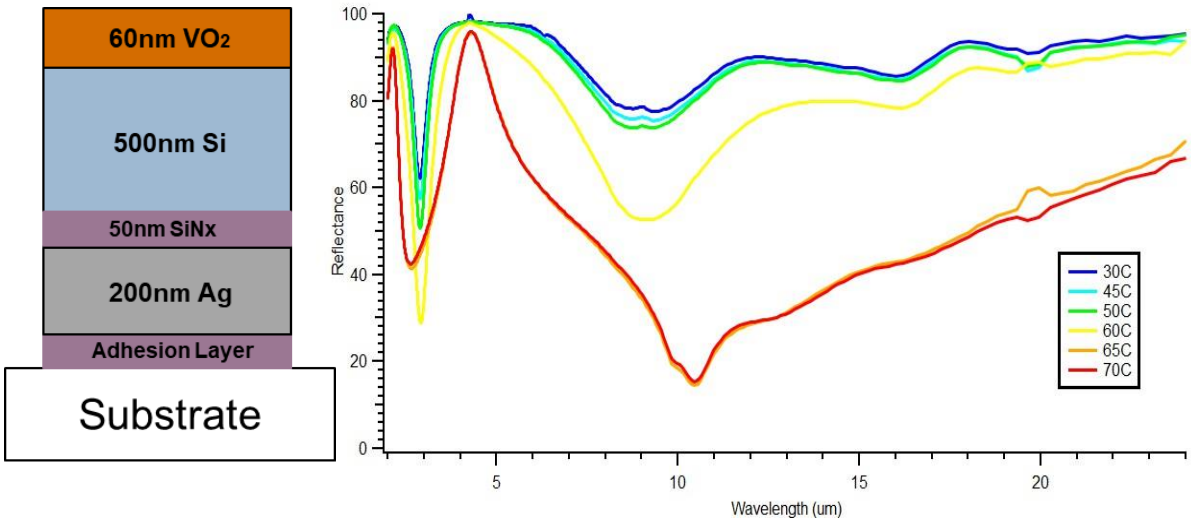

Figure 24: Reflectance spectra at varied temperatures of Si spacer VEM with a 60nm VO_2 top layer

The VEM with a VO_2 topping layer containing 1.2% Mo doping displays a significantly lower transition temperature below 40°C (Figure 25). The exact midpoint cannot be confirmed as the measurement setup was not able to reach cold enough temperatures (<15°C) to confirm a

stable insulating state. The Mo doped VEM transitions from 15°C or lower to a fully metallic state at 50°C. This transition range is much greater than the undoped sample which fully transition between 50°C to 65°C. From 15°C to 50°C, the Mo doped VEM is calculated to have a normal $\Delta\epsilon = 0.35$ but a true $\Delta\epsilon$ from a fully insulating to metallic state could not be calculated with the data measured.

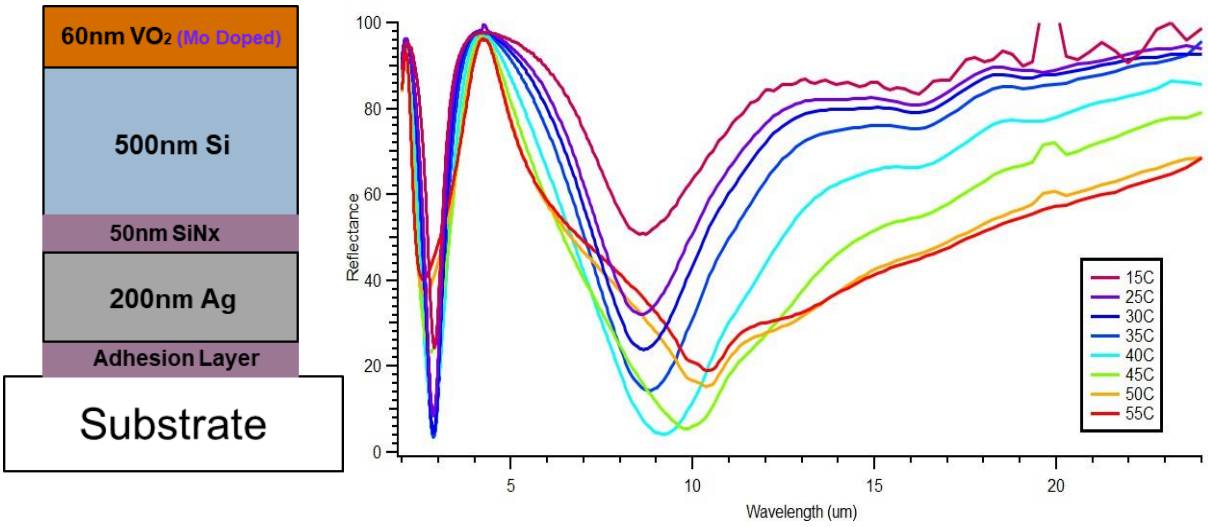

Figure 25: Reflectance spectra at varied temperatures of Si spacer VEM with a 60nm $V_{1-x}W_xO_2$ Top Layer.

In the experiments conducted, several VEM designs were successfully created, each featuring varying $\Delta\epsilon$ values. The thickness of the VO_2 layer and the choice of spacer material was observed to have a significant impact on the achievable $\Delta\epsilon$. Additionally, doping was found to reduce the transition temperature. Notably, limitations were identified in the modeled VO_2 properties due to thickness-dependent optical constants. The three-layer VEM design, consisting of a reflector, spacer, and VO_2 layers, demonstrated its capability in achieving a high $\Delta\epsilon$ value. However, the next objective was to investigate whether software optimization could further enhance this design beyond three layers.

4.6 Optimization of Design

TFcalc effectively optimized the thickness of a three-layer design using predetermined materials. The subsequent objective was to expand this optimization to include not only thickness but also the selection of materials and the number of layers in the design. A genetic optimizer was developed in MATLAB for this optimization.

The optimization of the 3-layer VEM design was initially performed using MATLAB's robust numerical solvers and optimization algorithms. The goal was to finely adjust the multilayer structure with the objective of maximizing the change in emissivity. The optimization process began with a predefined structure, which had already undergone experimental testing and demonstrated strong correlation with modeled designs due to the VO_2 optical constant's thickness dependency.

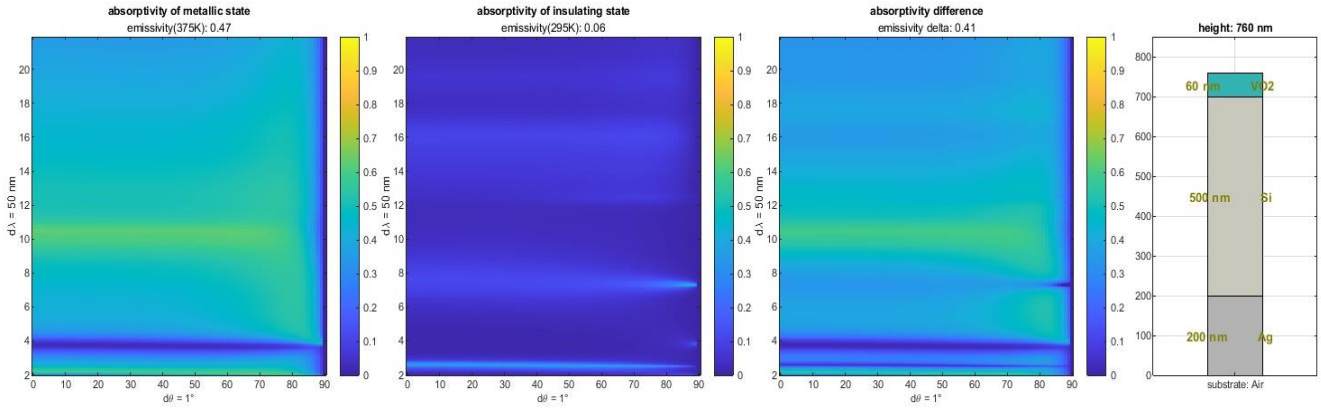

Figure 26: Simulation of 60nm VO_2 layer on 500nm Si with (left) angular emissivity vs wavelength with metallic VO_2 (middle) angular emissivity vs wavelength with insulating VO_2 (right) difference in angular emissivity between states. A normal $\Delta\epsilon$ =0.41 is achieved

This initial structure comprised a silver reflector, a 500nm silicon spacer, and a 60nm VO_2 topping layer. Figure 26 illustrates the absorptivity $(1 - R(\theta, \lambda))$ as a function of both wavelength and angle for the stack design. The left and middle plots represent the absorptivity for the structure when the VO_2 layer in its metallic and insulating states, respectively. The

corresponding emittance values for each state ($\epsilon_H = 0.47$, $\epsilon_L = 0.06$) are displayed above the plots and are calculated using Equation 7.

In the right plot, the wavelength, and angular dependencies of the difference in absorptivity between the two states are shown. Above the plot is displayed the change in emittance ($\Delta\epsilon$), which is calculated using Equation 7. This calculated $\Delta\epsilon = 0.41$ matched that achieved in TFCalc providing confidence in the MATLAB modeling.

The optimizer was subsequently given the flexibility to introduce a single layer composed of various materials as a topping layer above the VO_2 layer. The systematic adjustment of the thickness of this layer aimed to achieve the maximum $\Delta\epsilon$ (change in emissivity) between a configuration containing metallic VO_2 at 375K and one with insulating VO_2 at 295K. Consequently, a resulting optimized design successfully achieved a normal $\Delta\epsilon$ value of 0.65 by incorporating a 611nm thick silicon topping layer, as depicted in Figure 27.

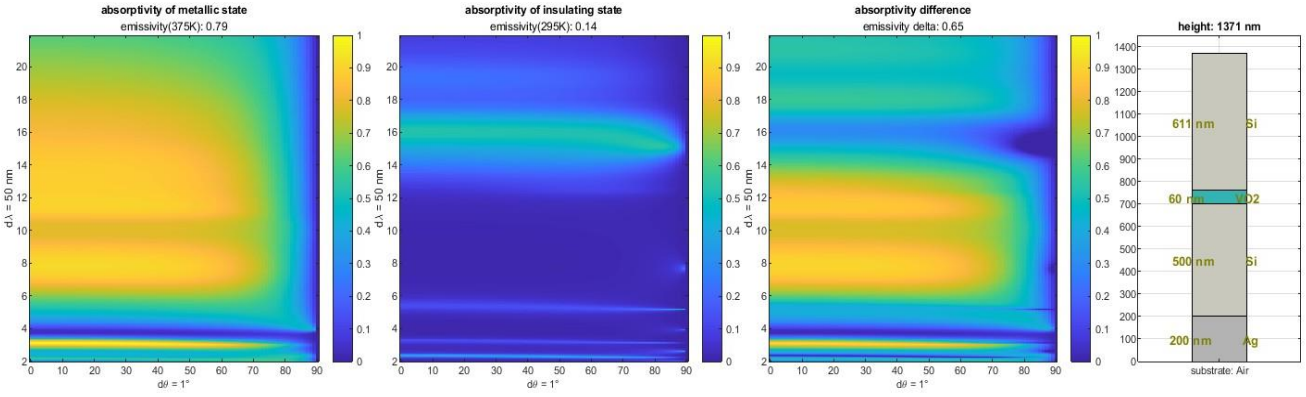

Figure 27: Simulation of 60nm VO_2 layer on 500nm Si with optimized single topping layer of 611nm Silicon (left) angular emissivity vs wavelength with metallic VO_2 (middle) angular emissivity vs wavelength with insulating VO_2 (right)difference in angular emissivity between states. A normal $\Delta\epsilon$ =0.65 is achieved

Next, the optimizer was empowered to add multiple layers on top of the VO_2 layer, again enabling material choice and thickness adjustments. The optimized design achieved a normal $\Delta\epsilon$ value of 0.79 by incorporating an enhancement stack of 600nm silicon layer followed by 900nm BaF_2 and a top layer of 79nm silicon, as depicted in Figure 28.

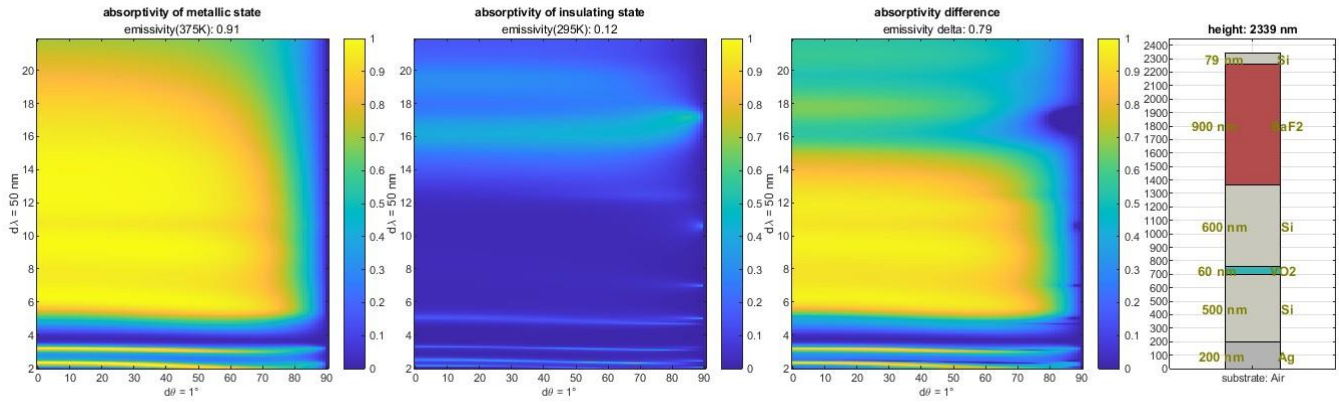

Figure 28: Simulation of 60nm VO_2 layer on 500nm Si with optimized multilayer of 600nm Si, 900nm BaF2, 79nm Si (left) angular emissivity vs wavelength with metallic VO_2 (middle) angular emissivity vs wavelength with insulating VO_2 (right) difference in angular emissivity between states. A normal $\Delta\epsilon$ =0.79 is achieved

Ultimately, the optimizer had the freedom to modify not just the initial silicon spacer's thickness and material composition, but also the thickness of the VO_2 layer during both single and multiple topping layer optimizations. In the case of single topping layer optimization, the optimizer opted once more for silicon as both the spacer and enhancement layer material. By setting the silicon spacer thickness at 443nm, the VO_2 layer thickness at 47nm, and introducing a silicon topping layer with a thickness of 562nm, a normal $\Delta\epsilon$ of 0.69 was attained as depicted in Figure 29.

During the multiple topping layer optimization, the optimizer chose a silicon spacer with a thickness of 505nm, a VO_2 layer with a thickness of 47nm, and introduced a three-layer topping structure consisting of 504nm of silicon, 897nm of BaF2, and 87nm of silicon. This

configuration achieved a remarkable and record-setting normal $\Delta\epsilon$ of 0.81 as depicted in Figure 30.

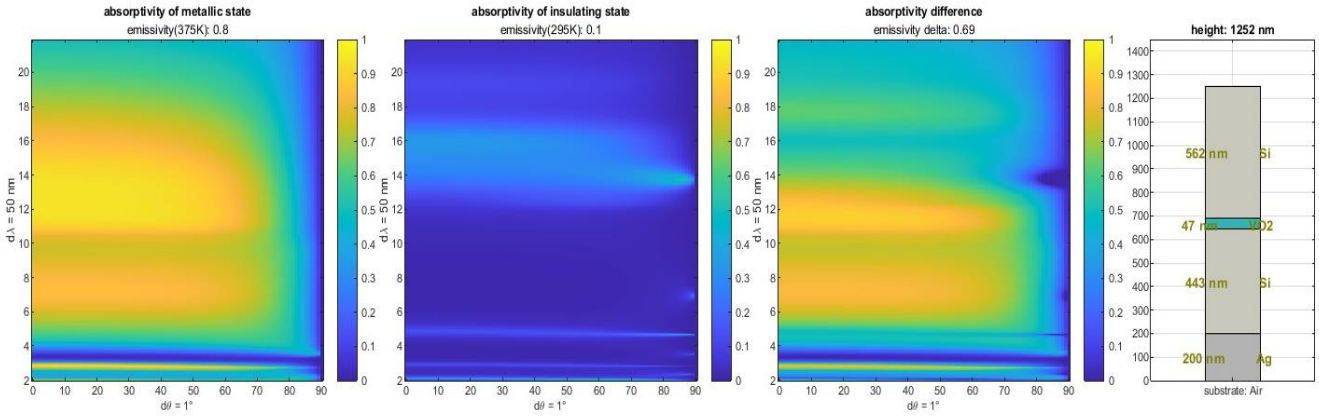

Figure 29: Simulation of 47nm VO_2 layer on 553nm Si with optimized single topping layer of 611nm Silicon (left) angular emissivity vs wavelength with metallic VO_2 (middle) angular emissivity vs wavelength with insulating VO_2 (right) difference in angular emissivity between states. A normal $\Delta\epsilon$ =0.69 is achieved

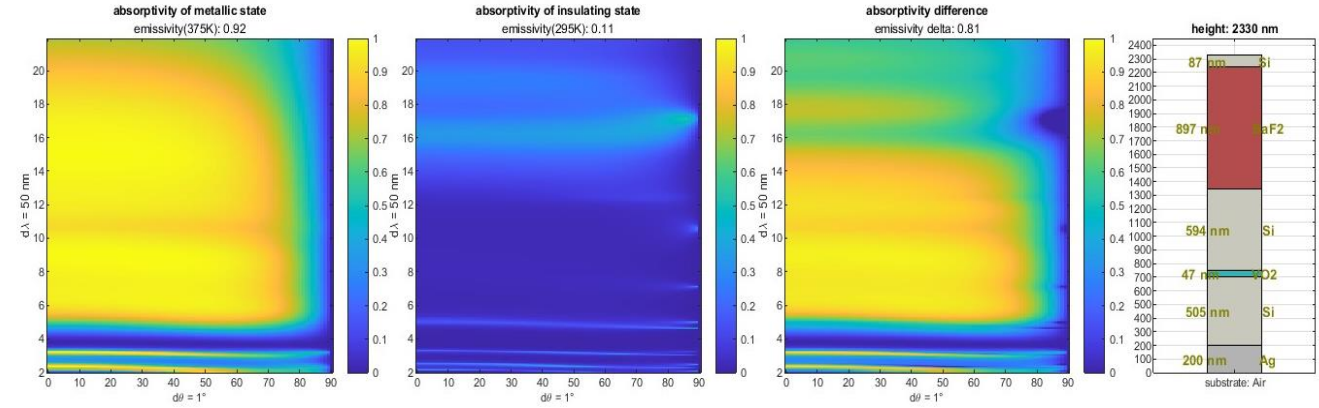

Figure 30: Simulation of 47nm VO_2 layer on 505nm Si with optimized multilayer of 594nm Si, 897nm BaF2, 87nm Si (left) angular emissivity vs wavelength with metallic VO_2 (middle) angular emissivity vs wavelength with insulating VO_2 (right)difference in angular emissivity between states. A normal $\Delta\epsilon$ =0.81 is achieved

The enhancement layers have successfully augmented absorption, thereby enhancing emissivity in the high-temperature metallic VO_2 VEM state, while maintaining the emissivity in the low-temperature insulating VO_2 VEM state near its original levels. This enhancement occurs due to a widening and amplification of the Fabry-Perot resonance peak, producing what this

study terms ‘broadband enhanced resonance.' This phenomenon is clearly demonstrated in the reflectance graph presented in Figure 31.

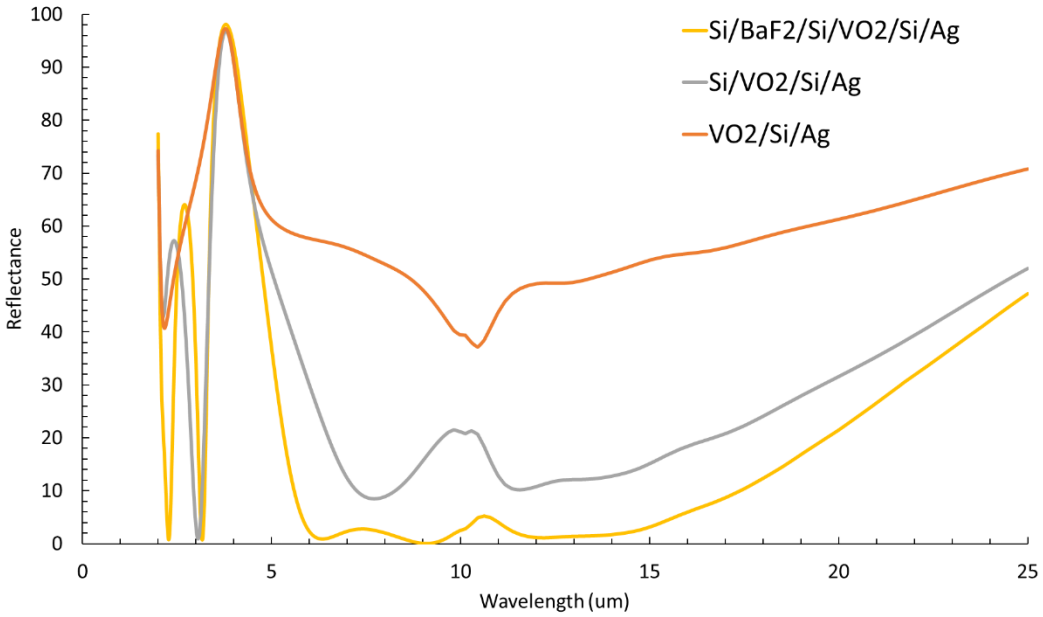

Figure 31: Modeled Reflectance of optimized VEM structures in the VO_2 metallic mode.

The ‘broadband enhanced resonance’ effect is attributed to the heightened normalized electric field within the VO_2 layer. This distinction is evident in Figure 32, which illustrates the squared normalized electric field intensity ($\mathcal{E}^2$) against wavelength within the VO_2 layer, comparing VEM with and without enhancement layers. The normalized electric field intensity ($\mathcal{E}^2$) was calculated in TFCalc. It is observable that the enhancement layers significantly amplify the electric field over a wide range of wavelengths. The amplification of the electric field in an absorbing layer increases the magnitude of absorbed energy in the layer, as shown in Equation 11.

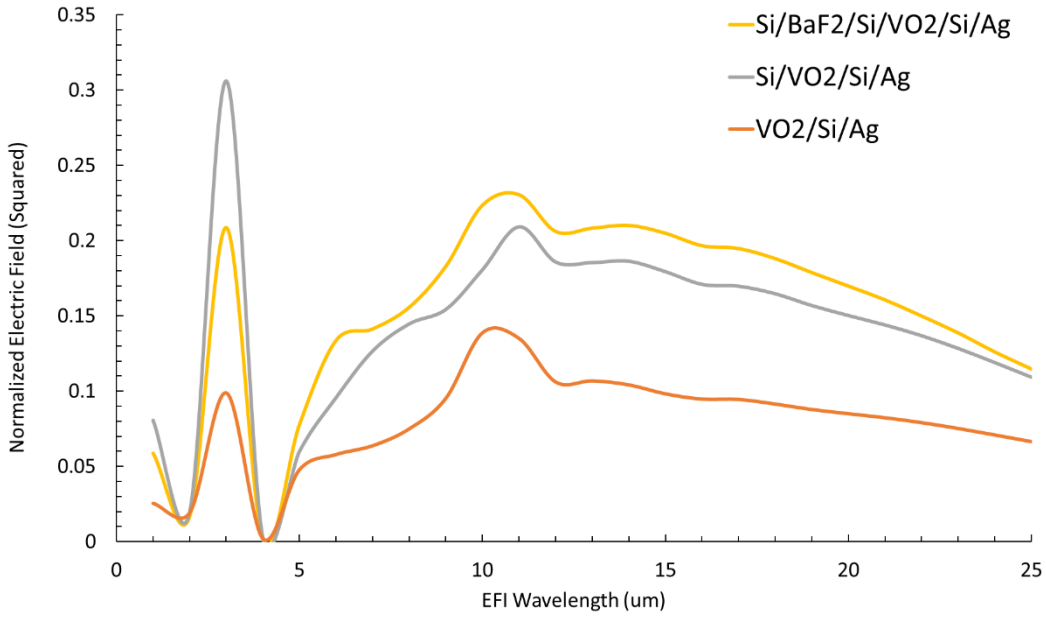

Figure 32: Normalized Electric Field in metallic VO_2 layer of optimized VEM structures.

It is postulated that the enhancement layer compresses the electric field further into the VO_2 layer, thus amplifying the electric field inside the VO_2 layer. In Figure 33, the plot of the squared peak of the normalized electric field ($\mathcal{E}^2$) at 10.5 µm versus the position in the VEM can be observed, comparing configurations with and without enhancement layers. The enhancement layers serve to heighten the electric field not only within the VO_2 layer but also within the silicon spacer layer.

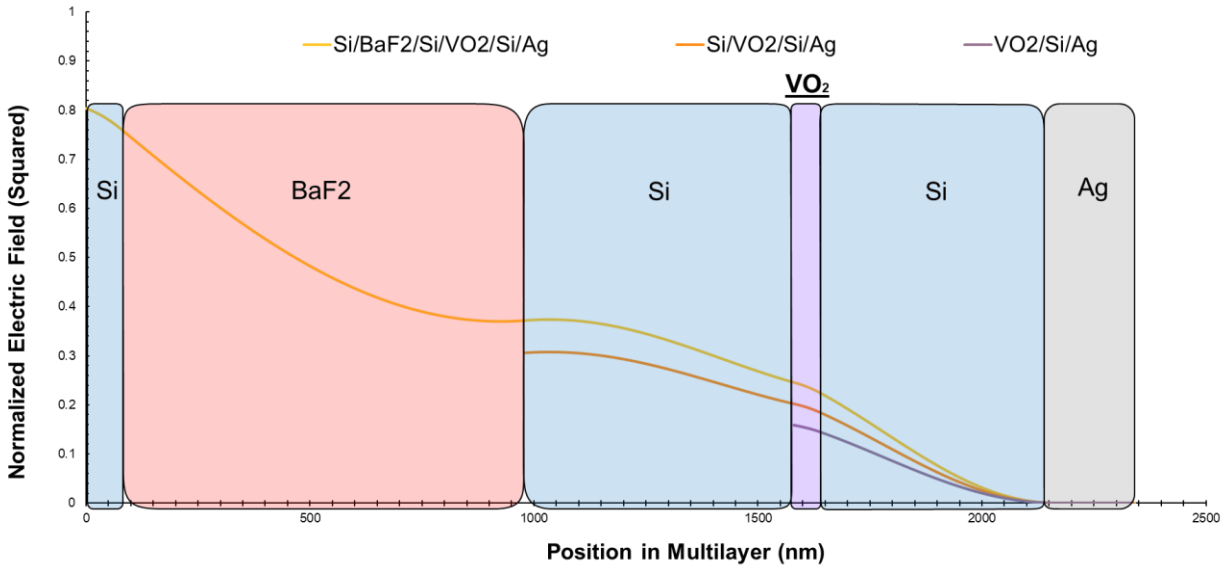

Figure 33: Diagram depicting Normalized Electric field versus the position inside of VEM of different enhancement layer stacks. The electric field was calculated at 10.5μm.

To summarize, the absorptance calculated from Figure 31 and the average $\mathcal{E}^2$ in the VO_2 calculated in Figures 32 and 33 at 10.5 μm are compared in Table 4. The improvement in the absorptance of the VED from the enhancement layers directly matches the improvement in the average $\mathcal{E}^2$ inside the VO_2 layer due the enhancement layers. This is not only true for 10.5 μm but for all wavelengths between 5 μm through 25 μm. The increased $\Delta\epsilon$ of the optimized VEM designs, due to 'broadband enhanced resonance' effect of the enhancement layers, is directly caused by the heightened normalized electric field within the VO_2 layer.

Table 4: VED absorptance compared to the average normalized electric field squared in VO_2 layer.

Design	Absorptance at 10.5 μm	% Improvement	Average $\mathcal{E}^2$ in VO_2 at 10.5um	% Improvement
VO_2/Si/Ag	0.625		0.156	
Si/VO_2/Si/Ag	0.800	28.0%	0.198	26.9%
Si/BaF_2/Si/VO_2/Si/Ag	0.950	52.0%	0.235	50.6%

4.7 Experimental Enhanced Broadband Resonance Layer

The optimization of the VEM design predicted that the addition of a few topping layers of the right material can create a broadband enhanced resonance and significantly increase the theoretical $\Delta\epsilon$ to some of the highest values ever reported. The final step in this project was fabrication of a VEM with a topping layer to achieve the predicted broadband enhanced resonance behavior. 600nm of silicon was sputtered onto a previously fabricated VEM design of 500nm silicon spacer and 60nm VO_2. The reflectance measurement of this multilayer is presented in Figure 34 and compared to the modeled data of the multilayer.

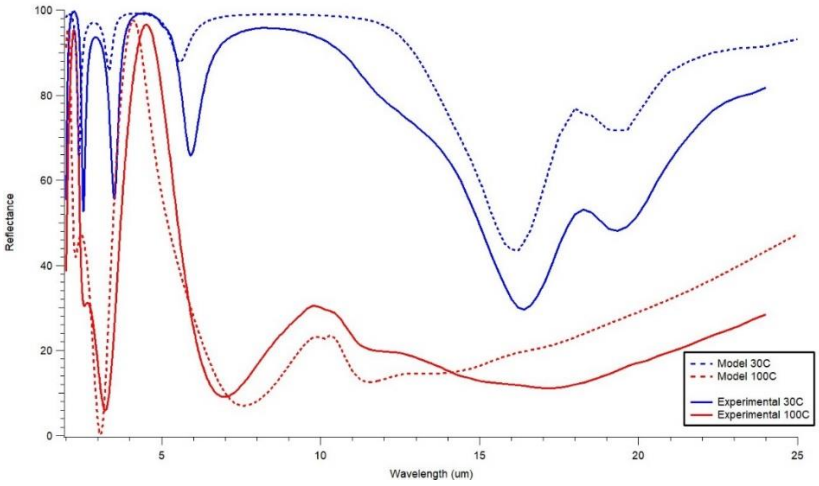

Figure 34: Simulated and Experimental Reflectance Spectra of Si enhancement layer on top of a VO_2 radiator design with a Si spacer layer.

At 100°C, the enhanced VEM exhibits a noteworthy broadband absorption pattern, in line with modelled predictions. The enhanced broadband resonance feature is observed starting from 7 µm all the way to 22 µm. This represents a substantial improvement from the VEM of the same design lacking an enhancement layer, demonstrated back in Figure 23, which only showed a peak resonance at 9 µm. Because of the enhanced broadband resonance, the emissivity of the

enhanced VEM at 100°C ϵ_H is 0.74. This is a 35% improvement as compared to the emissivity of VEM design at 100°C lacking the enhancement layer, $\epsilon_H = 0.55$.

Nonetheless, deviations from the model data persist in both the heated and unheated states, resulting in a diminished improvement to $\Delta\epsilon$. The emissivity's of both the cold insulating and hot metallic phase of the experimental VEM compared to the modeled VEM are presented in Table 5. The model initially predicted a normal $\Delta\epsilon$ of 0.65 for the enhanced VEM. This would mark a 58% improvement over the normal $\Delta\epsilon$ of VEM without an enhancement layer. In the experimental data, a normal $\Delta\epsilon$ of 0.50 was measured for the enhanced VEM. This represents a 16% improvement over the experimental normal $\Delta\epsilon$ value of fabricated VEM lacking an enhancement layer.

The experimental $\Delta\epsilon$ of 0.50 differs by 0.15 from the modeled $\Delta\epsilon$ of 0.65. Table 5 and Figure 34 demonstrate that a portion of this $\Delta\epsilon$ difference, specifically 0.03, can be attributed to discrepancies in the hot metallic phase (ϵ_H). This is influenced by the lower reflection between 8 µm and 13 µm in the modeled VEM. The primary source of the $\Delta\epsilon$ discrepancy, amounting to 0.12, stems from the variation in ϵ_L within the cold insulating phase. Figure 34 indicates that the experimental reflection is consistently lower than the modeled reflection from 6 µm to 25 µm, representing the significant disparity in ϵ_L. The higher broadband absorption in the cold insulating phase of the experimental device is the main cause of $\Delta\epsilon$ disparity between the experimental and modeled enhanced VEM.

Table 5: Emissivity at 300K and 375K of modelled and experimental enhanced VED

	ϵ_L (300K)	ϵ_H (375K)	$\Delta\epsilon = \epsilon_H - \epsilon_L$
Model	0.14	0.79	0.65
Experimental	0.26	0.76	0.50

Several factors may explain the observed discrepancies from the model. First is the confinement of VO_2 between two layers. Topping layers have been reported to limit stress relaxation of VO_2 due to geometrical confinement, potentially lowering the VO_2 transition temperature [105, 106]. If the cold insulating phase was already mid transition to the metallic phase, it would explain the lowered reflection as compared to the model.

To investigate this hypothesis, reflectance measurements were conducted on the enhanced VEM while varying the temperature from 30°C to 75°C, as shown in Figure 35. Interestingly, the VO_2 within the enhanced VEM does not exhibit a transition to the metallic phase until reaching temperatures between 60°C and 65°C, mirroring the behavior of the VEM lacking an enhancement layer. This is a standard temperature transition range for undoped VO_2 and suggests that geometrical confinement may not be a significant factor influencing the transition properties of VO_2.

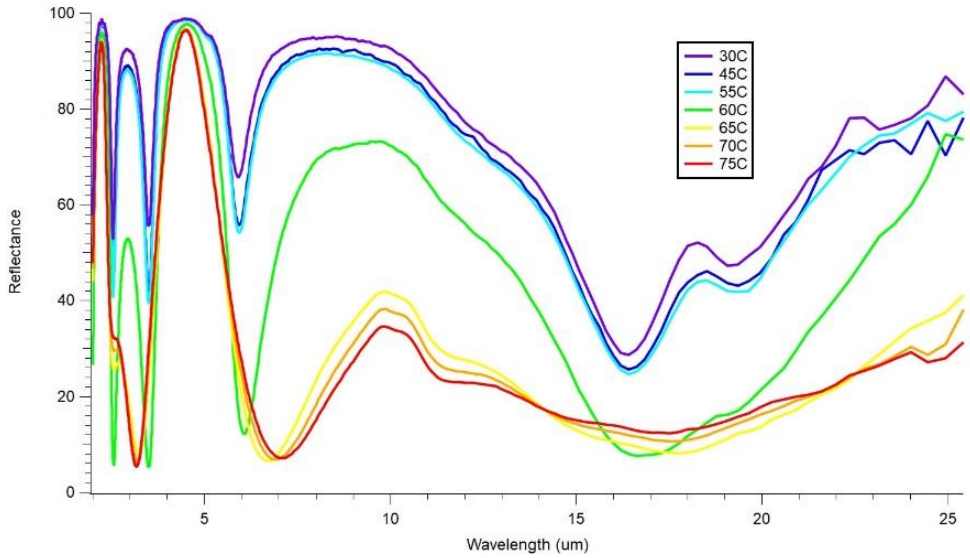

Figure 35: Reflectance spectra at varied temperatures of VEM with an enhancement layer

While it can be inferred that our enhanced VEM may not be in a mid-transition state within the cold insulating phase, it remains evident that the primary cause of the underachieved $\Delta\epsilon$ is the absorption in this phase. This may be due to absorption within the silicon due to the presence of oxygen. Not only are we doubling the thickness of sputtered a-Si in the device with the enhancement layer but the enhanced electric field in silicon spacer would increase pre-existing absorption effects.

Another consideration is increased absorption in the cold insulating VO_2(M) due to sputtering of the silicon enhancement layer. This include the possibility of interfacial effects and interdiffusion when silicon is deposited onto VO_2, potentially leading to increased absorption at lower temperatures, consequently limiting tunability [87, 89]. In previous studies, researchers utilized SiO_2 as a barrier layer on VO_2 when applying a silicon layer on top [87]. Another conjecture is that irradiation damage might have occurred at the surface of the VO_2 during the sputtering process for the silicon topping layer, as sputtering is an energetic process that could

have affected the stoichiometry or crystallinity of top VO_2 layers. Past research has demonstrated that thermochromic VO_2 can become amorphous due to ion bombardment [107]. To replicate the simulated results' $\Delta\epsilon$ performance in the experimental device, it is likely essential to have both a protected VO_2 film and sputtered silicon layers without the presence of oxygen to limit absorption in the cold insulating phase.

In conclusion, Figure 36 illustrates the observable experimental impact of the silicon enhancement layer. For the experimental 25nm and 60nm VO_2 topping layer VEMs, a narrow resonance peak passing below 20% reflectance is only observed near 9 µm and 10 µm respectively. For the experimental VEM with the enhancement layer, the resonance and low reflectance is broadband. The presence of the silicon enhancement layer results in a significant improvement in absorption and, consequently, an increase in the emissivity of the VEM within the 12-25 µm wavelength range.

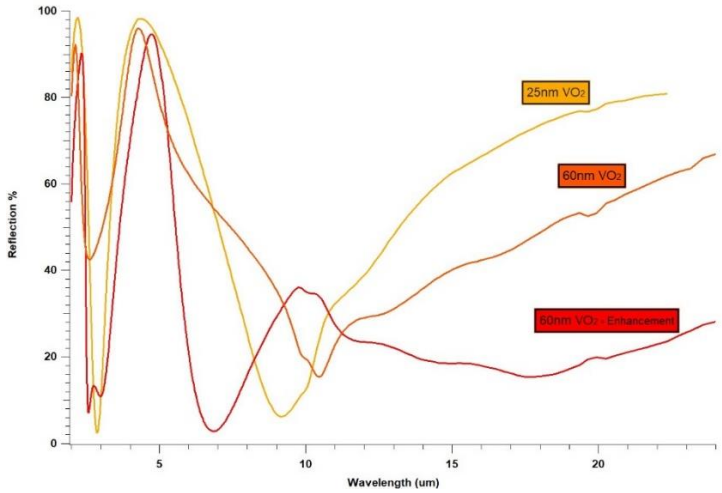

Figure 36: Reflectance spectra of experimental radiator devices with different VO_2 thickness and enhancement layer in metallic state.

5. Conclusion and Future Work

VO_2 was studied and synthesized with the goal of creating a variable emissive multilayer (VEM) utilizing the phase transition of VO_2 to achieve high emissivity at high temperature and low emissivity at low temperatures.

Thin films of highly oriented single phase VO_2(M) were successfully synthesized on a variety of substrates via magnetron sputtering deposition. Sputtered VO_2 films exhibited an 80% decrease in the transmittance in the NIR at 64°C as they transitioned from cold insulating VO_2(M) to hot metallic VO_2(R). This switch in the NIR affirmed a potential suitability for VEM use. UV, Visible and IR optical constants of a 60nm VO_2 film in both the insulating and metallic phase were measured with ellipsometry. The optical constants were then used for VEM modeling throughout the rest of the study.

Doping of VO_2 was studied with the goal of lowering the transition temperature. Introduction of molybdenum to VO_2 by co-sputtering was shown to lower the transition temperature by 13.3°C/at%. Introduction of tungsten was also measured to lower the transition temperature. Titanium doping was exhibited to increase the transition temperature and decrease the hysteresis width. It would be beneficial for future work to investigate the possibility of introducing multiple dopants to the VO_2 film with the goal of decreasing hysteresis width and transition temperature simultaneously.

A VEM utilizing a silver reflector, 1000nm SiO_2 spacer and 45nm VO_2 topping layer was measured to achieve a hemispherical emittance change ($\Delta\epsilon$) of 0.48 from 300K to 375K. The SiO_2 spacer displayed limitations in its use for maximizing $\Delta\epsilon$ due to its high absorption features. Because of this, silicon was studied as an alternative spacer material.

An experimental VEM, incorporating a silver reflector, a 500nm silicon spacer, and a 25nm VO_2 topping layer, yielded a normal $\Delta\epsilon$ of 0.44. Notably, this result deviated significantly from the modeled value of 0.55. The observed contrast between the experimental and modeled outcomes was attributed to the presence of oxygen in the sputter silicon spacer layer. Additionally, it was determined that the thickness-dependent nature of the optical constants of VO_2 played a role in this discrepancy. The optical constants measured for a 60nm VO_2 film were found to be unreliable when applied to a 25nm VO_2 film. It is recommended that future research investigates the optical constants of VO_2 across various thicknesses to gain insights into the evolution of both the refractive index (n) and extinction coefficient (k) with changing film thickness.

An experimental VEM, incorporating a silver reflector, a 500nm silicon spacer, and a 60nm VO_2 layer, exhibited a normal $\Delta\epsilon$ of 0.43 and demonstrated a transition temperature between 60°C and 65°C. The proximity of the experimental $\Delta\epsilon$ to the modeled value of 0.41 can be attributed to the use of a 60nm VO_2 film in the experimental setup, which more accurately represented the modeled optical constants of a 60nm VO_2 on a silicon substrate. The incorporation of 1.2% molybdenum into the VO_2 top film resulted in a decrease in the transition temperature of the VEM. However, accurate measurements of both the transition temperature and $\Delta\epsilon$ were hindered by the limitations of the measurement setup, which could not reach sufficiently low temperatures. Given the significance of reducing the transition temperatures of VO_2-based VEMs for real-world applications, future efforts should focus on developing a cold stage that enables precise measurements of transition temperature and $\Delta\epsilon$ at sub-300K temperatures.

A MATLAB optimizer was employed to maximize the achievable $\Delta\epsilon$ in a simulated VEM by introducing enhancement layers on top of the VO2 layer. The optimizer successfully attained a normal $\Delta\epsilon$ of 0.69 with the incorporation of a single silicon enhancement layer on top of a VEM comprising a silicon spacer and a 47nm VO2 film. Further improvement was achieved by adding a 3-layer topping structure consisting of Si-BaF2-Si to the Ag-Si-VO2 VEM, resulting in a groundbreaking theoretical normal $\Delta\epsilon$ of 0.81. This enhancement is attributed to the widening and amplification of the Fabry-Perot resonance peak, creating what this study terms a 'broadband enhanced resonance.' The enhancement is concluded to stem from an increase in the electric field within the VO_2 layer, as it is directly correlated to the absorption of the VEM.

An experimental demonstration featured a VEM with a silicon spacer, a 60nm VO_2 layer, and a 600nm silicon enhancement layer on top. The device exhibited a notable normal $\Delta\epsilon$ of 0.50 and showcased an enhanced broadband resonance in the hot metallic phase. This enhancement resulted in a remarkable 35% improvement in emissivity compared to the device lacking the silicon enhancement layer. This represents a substantial advancement in VEM design, and to the best of the author's knowledge, it marks the first reported experimental results of an enhancement layer.

The experimental enhanced VEM fell short of achieving the simulated normal $\Delta\epsilon$ of 0.65. This shortfall was attributed to absorption in the silicon layers, likely due to the presence of oxygen. Additionally, the degradation of the VO_2 layer following silicon sputtering on top contributed to the discrepancy. This underscores the critical importance of having accurate models for the silicon spacer material in this study. To address these issues, future research should involve IR ellipsometry measurements of the sputtered silicon material. Efforts should also be directed towards reducing oxygen presence in the silicon film to minimize absorption.

Furthermore, considering the potential degradation of the VO_2 film, a protective layer may be necessary before applying the enhancement layer. This protective layer would safeguard the VO_2 from degradation caused by ion bombardment or interdiffusion, which is crucial for minimizing absorption in the cold insulating phase and maximizing $\Delta\epsilon$. This work is crucial before further enhancement layers such as BaF_2 can be faithfully explored.

In conclusion, a powerful new design has been illuminated in this study to significantly improve the $\Delta\epsilon$ of VO_2 based variable emissive multilayers. The use of enhancement layers to achieve enhanced broadband resonance in the VO_2 VEM design not only have the power to significantly improve $\Delta\epsilon$ of the devices but will empower high $\Delta\epsilon$ as VEM designs move to lower transition temperatures due to the broadband resonance.

References

1. Fan, S., *Thermal Photonics and Energy Applications.* Joule, 2017. **1**(2): p. 264-273.
2. Raman, A.P., et al., *Passive radiative cooling below ambient air temperature under direct sunlight.* Nature, 2014. **515**(7528): p. 540-544.
3. Tang, K., et al., *Temperature-adaptive radiative coating for all-season household thermal regulation.* Science, 2021. **374**(6574): p. 1504-1509.
4. Taylor, S., et al., *Spectrally-selective vanadium dioxide based tunable metafilm emitter for dynamic radiative cooling.* Solar Energy Materials and Solar Cells, 2020. **217**: p. 110739.
5. Hendaoui, A., et al., *VO2-based smart coatings with improved emittance-switching properties for an energy-efficient near room-temperature thermal control of spacecrafts.* Solar Energy Materials and Solar Cells, 2013. **117**: p. 494-498.
6. Kim, H., et al., *VO(2)-based switchable radiator for spacecraft thermal control.* Sci Rep, 2019. **9**(1): p. 11329.
7. Haddad, E., et al., *Review of the VO2 smart material applications with emphasis on its use for spacecraft thermal control.* Frontiers in Materials, 2022. **9**.
8. KRUZELECKY, R.V., et al. *MULTIFUNCTION SMART COATINGS FOR SPACE APPLICATIONS*. 2006. Dordrecht: Springer Netherlands.
9. Wang, S., et al., *Scalable thermochromic smart windows with passive radiative cooling regulation.* Science, 2021. **374**(6574): p. 1501-1504.
10. Li, S.Y., G.A. Niklasson, and C.G. Granqvist, *Thermochromic fenestration with VO2-based materials: Three challenges and how they can be met.* Thin Solid Films, 2012. **520**(10): p. 3823-3828.
11. Morin, F.J., *Oxides Which Show a Metal-to-Insulator Transition at the Neel Temperature.* Physical Review Letters, 1959. **3**(1): p. 34-36.

12. Moatti, A., R. Sachan, and J. Narayan, *Volatile and non-volatile behavior of metal–insulator transition in VO2 through oxygen vacancies tunability for memory applications.* Journal of Applied Physics, 2020. **128**(4).

13. Ruzmetov, D., et al., *Three-terminal field effect devices utilizing thin film vanadium oxide as the channel layer.* Journal of Applied Physics, 2010. **107**(11).

14. Beaumont, A., et al., *Current-induced electrical self-oscillations across out-of-plane threshold switches based on VO2 layers integrated in crossbars geometry.* Journal of Applied Physics, 2014. **115**(15).

15. Hu, B., et al., *External-Strain Induced Insulating Phase Transition in VO2 Nanobeam and Its Application as Flexible Strain Sensor.* Advanced Materials, 2010. **22**(45): p. 5134-5139.

16. Jiang, J., G. Chugunov, and R.R. Mansour. *Fabrication and characterization of VO2-based series and parallel RF switches*. in *2017 IEEE MTT-S International Microwave Symposium (IMS)*. 2017.

17. Han, C., et al., *Broadband modulation of terahertz waves through electrically driven hybrid bowtie antenna-VO2 devices.* Scientific Reports, 2017. **7**(1): p. 12725.

18. Dönges, S.A., et al., *Ultrafast Nanoimaging of the Photoinduced Phase Transition Dynamics in VO2.* Nano Letters, 2016. **16**(5): p. 3029-3035.

19. Bowei, X., et al., *VO2-based superposed Fabry-Perot multilayer film with a highly enhanced infrared emittance and emittance tunability for spacecraft thermal control.* Optics Express, 2022. **30**(19): p. 34314-34327.

20. Griffiths, C.H. and H.K. Eastwood, *Influence of stoichiometry on the metal-semiconductor transition in vanadium dioxide.* Journal of Applied Physics, 1974. **45**(5): p. 2201-2206.

21. Cavalleri, A., et al., *Evidence for a structurally-driven insulator-to-metal transition in VO2: A view from the ultrafast timescale.* Physical Review B, 2004. **70**(16): p. 161102.

22. Whittaker, L., C.J. Patridge, and S. Banerjee, *Microscopic and Nanoscale Perspective of the Metal−Insulator Phase Transitions of VO2: Some New Twists to an Old Tale.* The Journal of Physical Chemistry Letters, 2011. **2**(7): p. 745-758.

23. Mott, N.F., *Metal-Insulator Transition.* Reviews of Modern Physics, 1968. **40**(4): p. 677-683.

24. Shao, Z., et al., *Recent progress in the phase-transition mechanism and modulation of vanadium dioxide materials.* NPG Asia Materials, 2018. **10**(7): p. 581-605.

25. Liu, K., et al., *Recent progresses on physics and applications of vanadium dioxide.* Materials Today, 2018. **21**(8): p. 875-896.

26. Outón, J., et al., *Tracking the optical constants of porous vanadium dioxide thin films during metal–insulator transition: Influence of processing conditions on their application in smart glasses.* Applied Surface Science, 2022. **580**: p. 152228.

27. Goodenough, J.B., *The two components of the crystallographic transition in VO2.* Journal of Solid State Chemistry, 1971. **3**(4): p. 490-500.

28. Lee, S., et al., *Epitaxial stabilization and phase instability of VO2 polymorphs.* Scientific Reports, 2016. **6**(1): p. 19621.

29. Yang, Z., et al., *Dielectric and carrier transport properties of vanadium dioxide thin films across the phase transition utilizing gated capacitor devices.* Physical Review B, 2010. **82**(20): p. 205101.

30. Lee, S., et al., *Anomalously low electronic thermal conductivity in metallic vanadium dioxide.* Science, 2017. **355**(6323): p. 371-374.

31. Barker, A.S., H.W. Verleur, and H.J. Guggenheim, *Infrared Optical Properties of Vanadium Dioxide Above and Below the Transition Temperature.* Physical Review Letters, 1966. **17**(26): p. 1286-1289.

32. Cavalleri, A., et al., *Femtosecond Structural Dynamics in ${\mathrm{VO}}_{2}$ during an Ultrafast Solid-Solid Phase Transition.* Physical Review Letters, 2001. **87**(23): p. 237401.

33. Stefanovich, G., A. Pergament, and D. Stefanovich, *Electrical switching and Mott transition in VO2.* Journal of Physics: Condensed Matter, 2000. **12**(41): p. 8837.

34. Kim, J. and T. Paik, *Recent Advances in Fabrication of Flexible, Thermochromic Vanadium Dioxide Films for Smart Windows.* Nanomaterials, 2021. **11**(10).

35. Zheng, J., S. Bao, and P. Jin, *TiO2(R)/VO2(M)/TiO2(A) multilayer film as smart window: Combination of energy-saving, antifogging and self-cleaning functions.* Nano Energy, 2015. **11**: p. 136-145.

36. Zhou, J., et al., *VO2 thermochromic smart window for energy savings and generation.* Scientific Reports, 2013. **3**(1): p. 3029.

37. Chang, T.-C., et al., *Review on thermochromic vanadium dioxide based smart coatings: from lab to commercial application.* Advances in Manufacturing, 2018. **6**(1): p. 1-19.

38. Théry, V., et al., *Role of thermal strain in the metal-insulator and structural phase transition of epitaxial ${\mathrm{VO}}_{2}$ films.* Physical Review B, 2016. **93**(18): p. 184106.

39. Xu, G., et al., *Thickness dependence of optical properties of VO2 thin films epitaxially grown on sapphire (0001).* Applied Surface Science, 2005. **244**(1): p. 449-452.

40. Yang, Y., et al., *Transmittance change with thickness for polycrystalline VO2 films deposited at room temperature.* Journal of Alloys and Compounds, 2019. **791**: p. 648-654.

41. Jian, J., et al., *Continuous Tuning of Phase Transition Temperature in VO2 Thin Films on c-Cut Sapphire Substrates via Strain Variation.* ACS Applied Materials & Interfaces, 2017. **9**(6): p. 5319-5327.

42. Zhou, H., et al., *Optical and electrical switching properties of VO2 thin film on MgF2 (111) substrate.* Ceramics International, 2016. **42**(6): p. 7655-7663.

43. Nagashima, K., et al., *Stress relaxation effect on transport properties of strained vanadium dioxide epitaxial thin films.* Physical Review B, 2006. **74**(17): p. 172106.

44. Molaei, R., et al., *A microstructural approach toward the effect of thickness on semiconductor-to-metal transition characteristics of VO2 epilayers.* Journal of Applied Physics, 2014. **115**(16): p. 164311.

45. Futaki, H. and M. Aoki, *Effects of Various Doping Elements on the Transition Temperature of Vanadium Oxide Semiconductors.* Japanese Journal of Applied Physics, 1969. **8**(8): p. 1008-1013.

46. Aetukuri, N.B., et al., *Control of the metal–insulator transition in vanadium dioxide by modifying orbital occupancy.* Nature Physics, 2013. **9**(10): p. 661-666.

47. Yano, A., et al., *Toward High-Precision Control of Transformation Characteristics in VO2 through Dopant Modulation of Hysteresis.* The Journal of Physical Chemistry C, 2020. **124**(39): p. 21223-21231.

48. Krammer, A., et al., *Elevated transition temperature in Ge doped VO2 thin films.* Journal of Applied Physics, 2017. **122**(4): p. 045304.

49. Jin, P. and S.T. Sakae Tanemura, *Relationship between Transition Temperature and x in V1-xWxO2 Films Deposited by Dual-Target Magnetron Sputtering.* Japanese Journal of Applied Physics, 1995. **34**(5R): p. 2459.

50. Wan, C., et al., *On the Optical Properties of Thin-Film Vanadium Dioxide from the Visible to the Far Infrared.* Annalen der Physik, 2019. **531**(10): p. 1900188.

51. Nag, J. and R.F. Haglund Jr, *Synthesis of vanadium dioxide thin films and nanoparticles.* Journal of Physics: Condensed Matter, 2008. **20**(26): p. 264016.

52. Malarde, D., et al., *Optimized Atmospheric-Pressure Chemical Vapor Deposition Thermochromic VO2 Thin Films for Intelligent Window Applications.* ACS Omega, 2017. **2**(3): p. 1040-1046.

53. Shibuya, K. and A. Sawa, *Optimization of conditions for growth of vanadium dioxide thin films on silicon by pulsed-laser deposition.* AIP Advances, 2015. **5**(10): p. 107118.

54. Maaza, M., et al., *Direct production of thermochromic VO2 thin film coatings by pulsed laser ablation.* Optical Materials, 2000. **15**(1): p. 41-45.

55. Fuls, E.N., D.H. Hensler, and A.R. Ross, *Reactively Sputtered Vanadium Dioxide Thin Films.* Applied Physics Letters, 1967. **10**(7): p. 199-201.

56. Zhang, C., et al., *Characterization of vanadium oxide thin films with different stoichiometry using Raman spectroscopy.* Thin Solid Films, 2016. **620**: p. 64-69.

57. Mlyuka, N.R. and R.T. Kivaisi, *Correlation between optical, electrical and structural properties of vanadium dioxide thin films.* Journal of Materials Science, 2006. **41**(17): p. 5619-5624.

58. Gagaoudakis, E., et al., *Low-temperature rf sputtered VO2 thin films as thermochromic coatings for smart glazing systems.* Solar Energy, 2018. **165**: p. 115-121.

59. Ruzmetov, D., et al., *Correlation between metal-insulator transition characteristics and electronic structure changes in vanadium oxide thin films.* Physical Review B, 2008. **77**(19): p. 195442.

60. Sirjita, E.-N., et al., *Structural and electrical properties of high-performance vanadium dioxide thin layers obtained by reactive magnetron sputtering.* Thin Solid Films, 2022. **759**: p. 139461.

61. Ruzmetov, D., S.D. Senanayake, and S. Ramanathan, *X-ray absorption spectroscopy of vanadium dioxide thin films across the phase-transition boundary.* Physical Review B, 2007. **75**(19): p. 195102.

62. Jin, P. and S. Tanemura, *V1−xMoxO2 thermochromic films deposited by reactive magnetron sputtering.* Thin Solid Films, 1996. **281-282**: p. 239-242.

63. Hanlon, T.J., J.A. Coath, and M.A. Richardson, *Molybdenum-doped vanadium dioxide coatings on glass produced by the aqueous sol–gel method.* Thin Solid Films, 2003. **436**(2): p. 269-272.

64. Lee, M.-H., et al., *Controlling Metal–Insulator Transitions in Vanadium Oxide Thin Films by Modifying Oxygen Stoichiometry.* ACS Applied Materials & Interfaces, 2021. **13**(1): p. 887-896.

65. Brassard, D., et al., *Grain size effect on the semiconductor-metal phase transition characteristics of magnetron-sputtered VO2 thin films.* Applied Physics Letters, 2005. **87**(5).

66. Ruzmetov, D., et al., *Structure-functional property relationships in rf-sputtered vanadium dioxide thin films.* Journal of Applied Physics, 2007. **102**(11).

67. Jian, J., et al., *Roles of grain boundaries on the semiconductor to metal phase transition of VO2 thin films.* Applied Physics Letters, 2015. **107**(10).

68. Mlyuka, N.R., G.A. Niklasson, and C.G. Granqvist, *Thermochromic multilayer films of VO2 and TiO2 with enhanced transmittance.* Solar Energy Materials and Solar Cells, 2009. **93**(9): p. 1685-1687.

69. Gan, F.Y. and P. Laou, *Optical and electrical properties of sputtered vanadium oxide films.* Journal of Vacuum Science & Technology A, 2004. **22**(3): p. 879-882.

70. Kreith, F., R.M. Manglik, and M.S. Bohn, *Principles of Heat Transfer*. 2010: Cengage Learning.

71. Neu, J., *Measurement of hemispherical directional reflectance in the infrared*. SPIE's 1993 International Symposium on Optics, Imaging, and Instrumentation. Vol. 1995. 1993: SPIE.

72. Ramirez-Rincon, J.A., et al., *Thermal hysteresis measurement of the VO2 dielectric function for its metal-insulator transition by visible-IR ellipsometry.* Journal of Applied Physics, 2018. **124**(19).

73. De Sousa Meneses, D., M. Malki, and P. Echegut, *Structure and lattice dynamics of binary lead silicate glasses investigated by infrared spectroscopy.* Journal of Non-Crystalline Solids, 2006. **352**(8): p. 769-776.

74. Perot, A. and C. Fabry, *On the Application of Interference Phenomena to the Solution of Various Problems of Spectroscopy and Metrology.* The Astrophysical Journal, 1899. **9**: p. 87.

75. Vaughan, M., *The Fabry-Perot Interferometer: History, Theory, Practice and Applications*. 2017: CRC Press.

76. Shu, S., Z. Li, and Y.Y. Li, *Triple-layer Fabry-Perot absorber with near-perfect absorption in visible and near-infrared regime.* Optics Express, 2013. **21**(21): p. 25307-25315.

77. Kats, M.A., et al., *Ultra-thin perfect absorber employing a tunable phase change material.* Applied Physics Letters, 2012. **101**(22).

78. Taylor, S., Y. Yang, and L. Wang, *Vanadium dioxide based Fabry-Perot emitter for dynamic radiative cooling applications.* Journal of Quantitative Spectroscopy and Radiative Transfer, 2017. **197**: p. 76-83.

79. Rancourt, J.D., *Optical Thin Films: User Handbook*. 1996: SPIE Optical Engineering Press.

80. Celanovic, I., D. Perreault, and J. Kassakian, *Resonant-cavity enhanced thermal emission.* Physical Review B, 2005. **72**(7): p. 075127.

81. Beaini, R., et al., *Thermochromic VO2-based smart radiator devices with ultralow refractive index cavities for increased performance.* Solar Energy Materials and Solar Cells, 2020. **205**: p. 110260.

82. Hendaoui, A., et al., *Highly tunable-emittance radiator based on semiconductor-metal transition of VO2 thin films.* Applied Physics Letters, 2013. **102**(6).

83. Kim, H., et al., *VO2-based thin-film radiators with variable thermal emissivity.* Thin Solid Films, 2022. **759**: p. 139455.

84. Wang, X., et al., *Fabrication of VO2-based multilayer structure with variable emittance.* Applied Surface Science, 2015. **344**: p. 230-235.

85. Zhang, D., et al., *Spacecraft smart radiation device with variable emission and low absorption based on phase change material VO2.* International Journal of Thermal Sciences, 2023. **185**: p. 108039.

86. Wu, B., et al., *An efficient optimization strategy applied to spacecraft smart radiation devices design.* International Journal of Thermal Sciences, 2024. **195**: p. 108635.

87. Hendaoui, A., et al., *Enhancement of the positive emittance-switching performance of thermochromic VO2 films deposited on Al substrate for an efficient passive thermal control of spacecrafts.* Current Applied Physics, 2013. **13**(5): p. 875-879.

88. Wu, B., et al., *Spacecraft smart radiation device with near-zero solar absorption based on cascaded photonic crystals.* Case Studies in Thermal Engineering, 2023. **50**: p. 103473.

89. Hendaoui, A., *Low Solar Absorptance, High Emittance Performance Thermochromic VO2-Based Smart Radiator Device.* Nanomaterials, 2022. **12**(24): p. 4422.

90. Woolf, D.N., et al. *Combining Sol-Gel and Evaporative Coating Techniques to Produce High-Solar Reflectivity, High-Contrast Variable Emissivity Coatings using Vanadium Dioxide*. in *Optical Interference Coatings Conference (OIC) 2022*. 2022. Whistler, British Columbia: Optica Publishing Group.

91. Zhang, K., et al., *A theoretical study on the effect of protective layer on the solar absorption and infrared emittance of spacecraft smart thermal control devices.* Optics & Laser Technology, 2024. **169**: p. 110087.

92. Macleod, H.A., *Thin-Film Optical Filters*. Third Edition ed. 2001, Bristol and Philadephia: Institue of Physics Publishing.

93. Chandler-Horowitz, D. and P.M. Amirtharaj, *High-accuracy, midinfrared (450cm−1⩽ω⩽4000cm−1) refractive index values of silicon.* Journal of Applied Physics, 2005. **97**(12).

94. Querry, M.R., *Optical Constants of Minerals and Other Materials from Millimeter to the Ultraviolet*. 1987, CRDEC.

95. Yang, H.U., et al., *Optical dielectric function of silver.* Physical Review B, 2015. **91**(23): p. 235137.

96. McDonnell, J.R. and R.G. Reynolds, *Evolutionary Programming IV: Proceedings of the Fourth Annual Conference on Evolutionary Programming*. 1995: MIT Press.

97. Li Voti, R., *Optimization of a perfect absorber multilayer structure by genetic algorithms.* Journal of the European Optical Society-Rapid Publications, 2018. **14**(1): p. 11.

98. Bloom, A.L., *Refining and optimization in multilayers.* Applied Optics, 1981. **20**(1): p. 66-73.

99. Depla, D., J. Haemers, and R. De Gryse, *Discharge voltage measurements during reactive sputtering of oxides.* Thin Solid Films, 2006. **515**(2): p. 468-471.

100. Kübler, C., et al., *Coherent Structural Dynamics and Electronic Correlations during an Ultrafast Insulator-to-Metal Phase Transition in ${\mathrm{VO}}_{2}$.* Physical Review Letters, 2007. **99**(11): p. 116401.

101. Béteille, F., et al., *Switching properties of V1 − xTixO2 thin films deposited from alkoxides.* Materials Research Bulletin, 1997. **32**(8): p. 1109-1117.

102. Takahashi, I., M. Hibino, and T. Kudo, *Thermochromic Properties of Double-Doped VO2 Thin Films Prepared by a Wet Coating Method Using Polyvanadate-Based Sols Containing W and Mo or W and Ti.* Japanese Journal of Applied Physics, 2001. **40**(3R): p. 1391.

103. Herguedas, N. and E. Carretero, *Optical Properties in Mid-Infrared Range of Silicon Oxide Thin Films with Different Stoichiometries.* Nanomaterials, 2023. **13**(20): p. 2749.

104. Zhao, J.H., et al., *Investigation of interfacial phenomena in Ag–Si multilayers during the annealing process.* Journal of Materials Research, 1999. **14**(7): p. 2888-2892.

105. Kakiuchida, H., P. Jin, and M. Tazawa, *Control of Optical Performance in Infrared Region for Vanadium Dioxide Films Layered by Amorphous Silicon.* International Journal of Thermophysics, 2010. **31**(10): p. 1964-1971.

106. Viswanath, C.K., B., Z. Yang, and S. Ramanathan, *Geometric confinement effects on the metal-insulator transition temperature and stress relaxation in VO2 thin films grown on silicon.* Journal of Applied Physics, 2011. **109**(6).

107. Rensberg, J., et al., *Active Optical Metasurfaces Based on Defect-Engineered Phase-Transition Materials.* Nano Letters, 2016. **16**(2): p. 1050-1055.